united nations
educational, scientific
and cultural
organization

international atomic
energy agency

the
abdus salam
international centre for theoretical physics

SMR 1331/23

AUTUMN COLLEGE ON PLASMA PHYSICS

8 October - 2 November 2001

AURORAL ZONE PLASMA PHYSICS
Appendix

Robert L. Lysak
University of Minnesota, U.S.A.

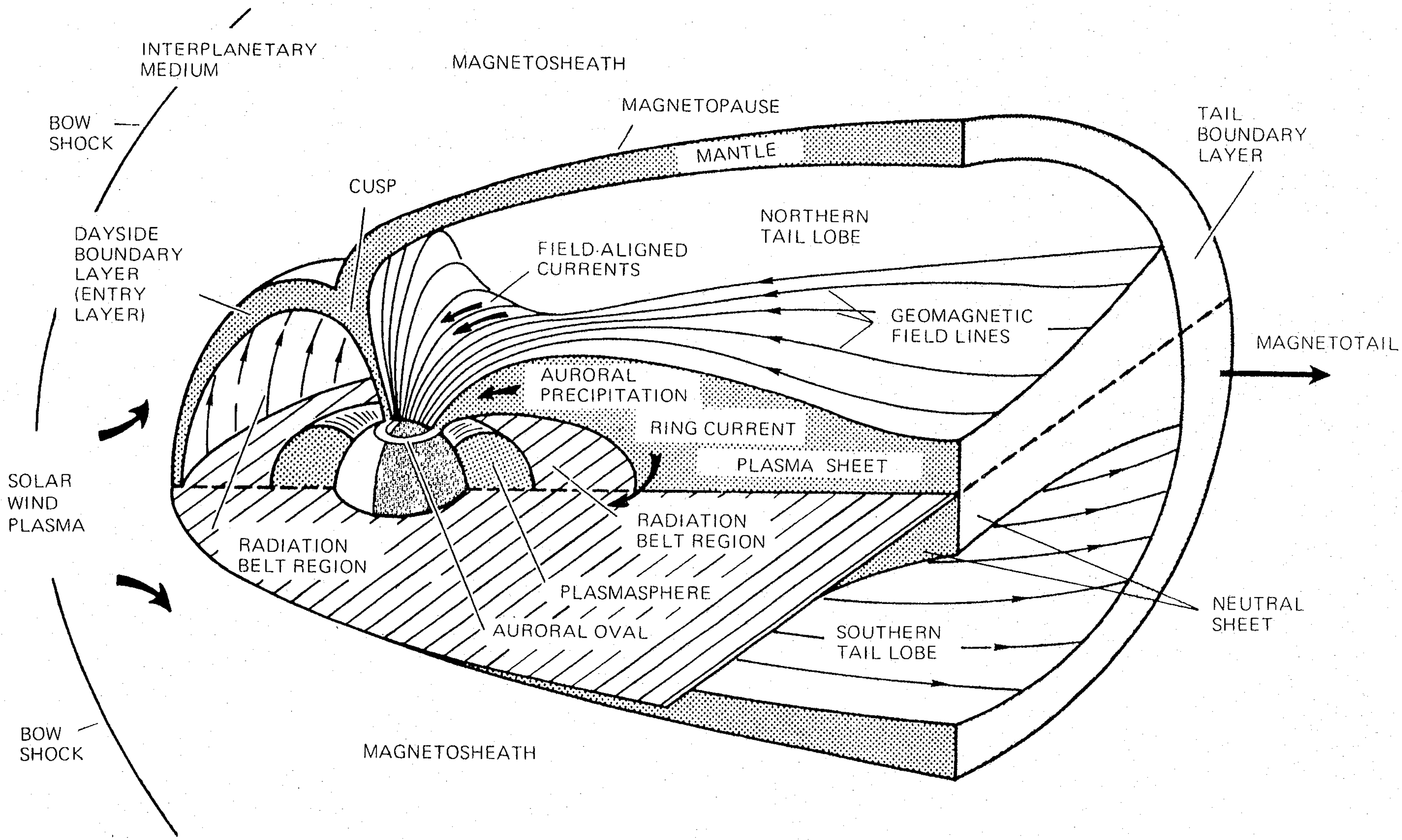

Fig. 1.13. Schematic representation of the magnetosphere. (Courtesy of J. Roederer.)

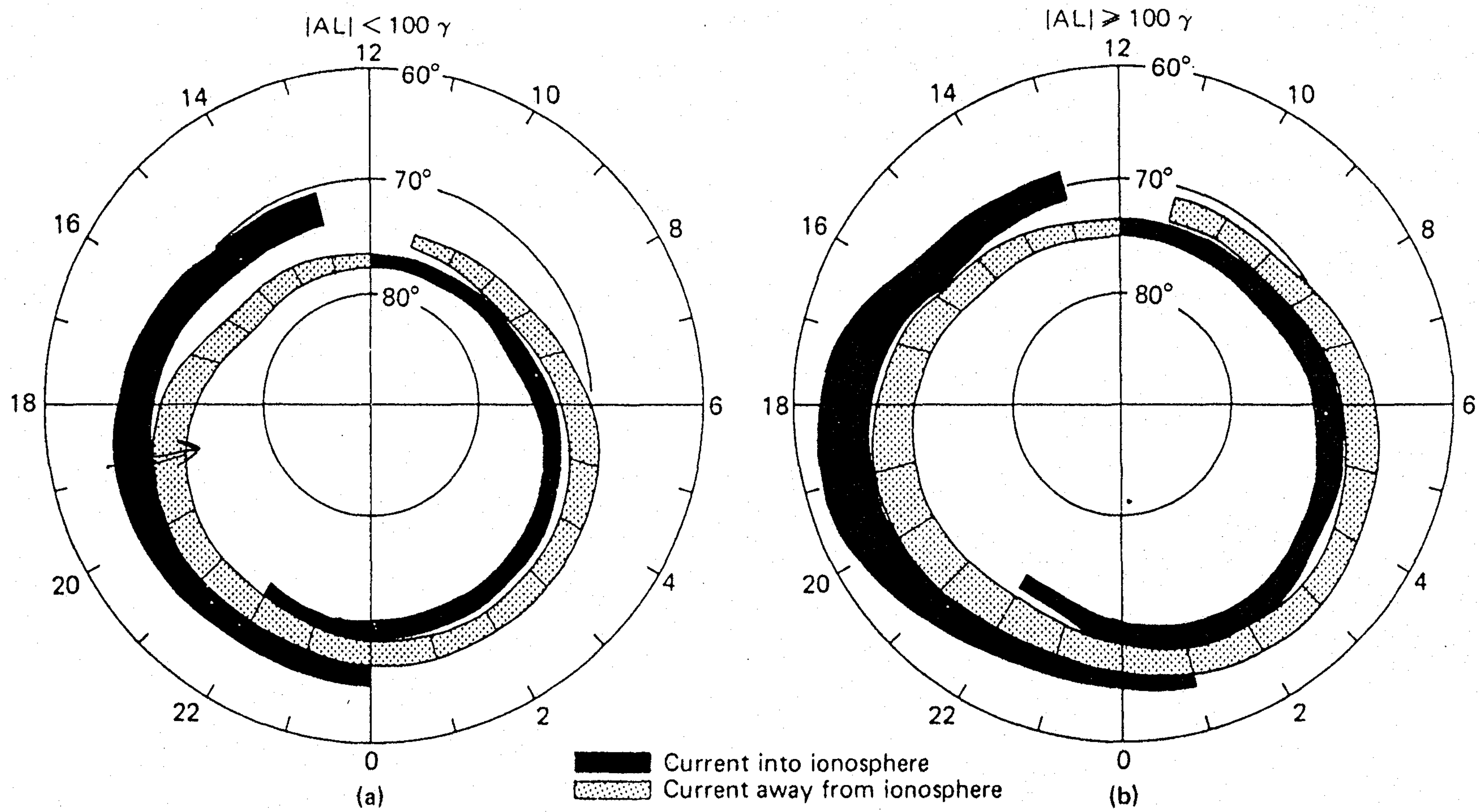

Fig. 13. A summary of the distribution and flow directions of large-scale field-aligned currents determined from (*a*) data obtained from 439 passes of Triad during weakly disturbed conditions ($|AL| < 100\ \gamma$) and (*b*) data obtained from 366 Triad passes during active periods ($|AL| \geq 100\ \gamma$).

netometers must be primarily driven by a magnetospheric generator because a larger amount of energy, which is presumably available for the generation of field-aligned currents, is stored in the magnetosphere than in the ionosphere. The auroral ionosphere must, however, play a secondary role in the

We suggest that the appearance of complicated small-scale structures on the nightside during substorm activity is closely associated with the changes in the magnetotail plasma sheet such as its thinning, constriction, and expansion [e.g., *Hones,* 1973], the switching of bulk flow direction of hot components increases. In the example shown the spectral peak is at 2 'or a 0° spectrum but is at 3 keV for a 45° spectrum. *Ar- et al.* [1974] discuss exactly this behavior on the part of)served auroral electron beam.

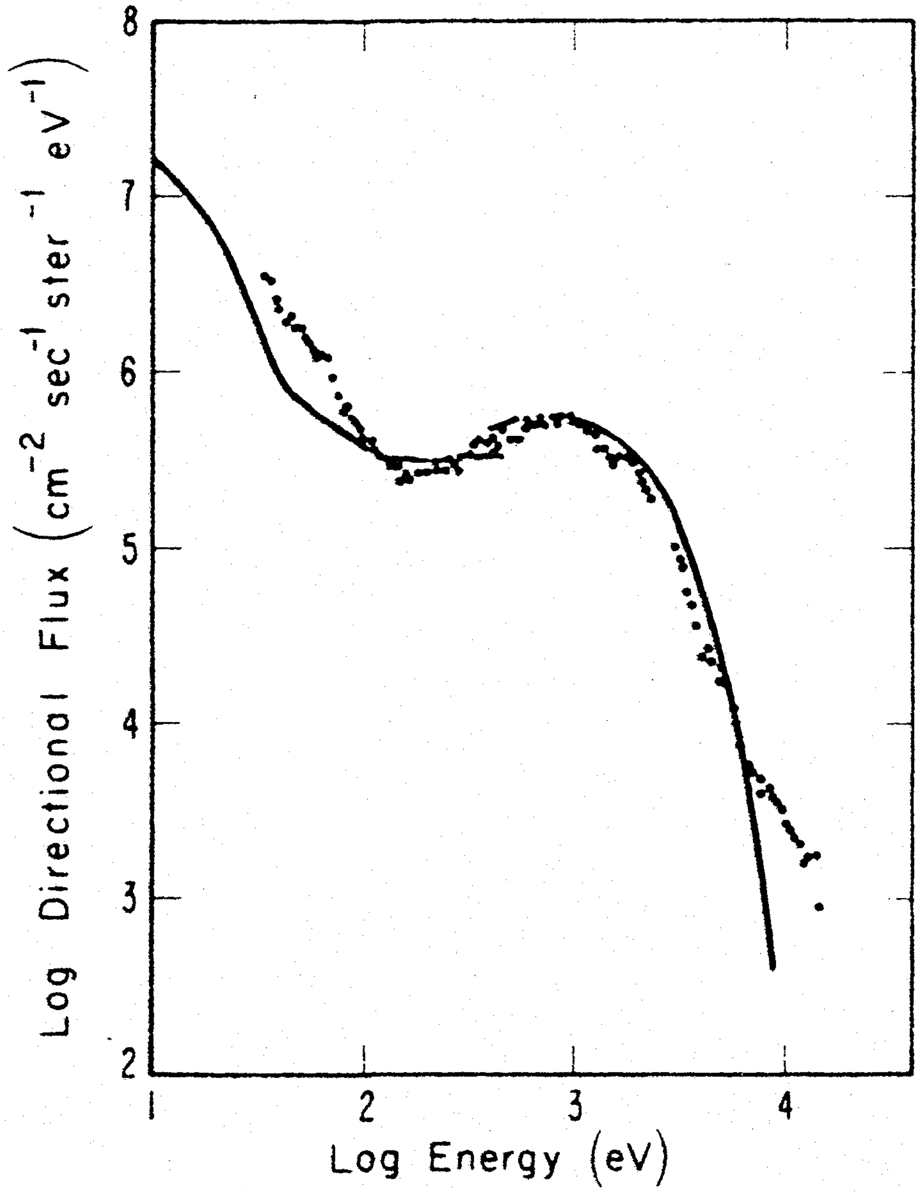

:. 7. Model electron energy spectrum computed by assuming a ' potential difference along a magnetic field line and an un- ized Maxwellian electron distribution of temperature of 800 eV density of 5 cm $^{-3}$. The data represent an electron spectrum ved by *Frank and Ackerson* [1971].

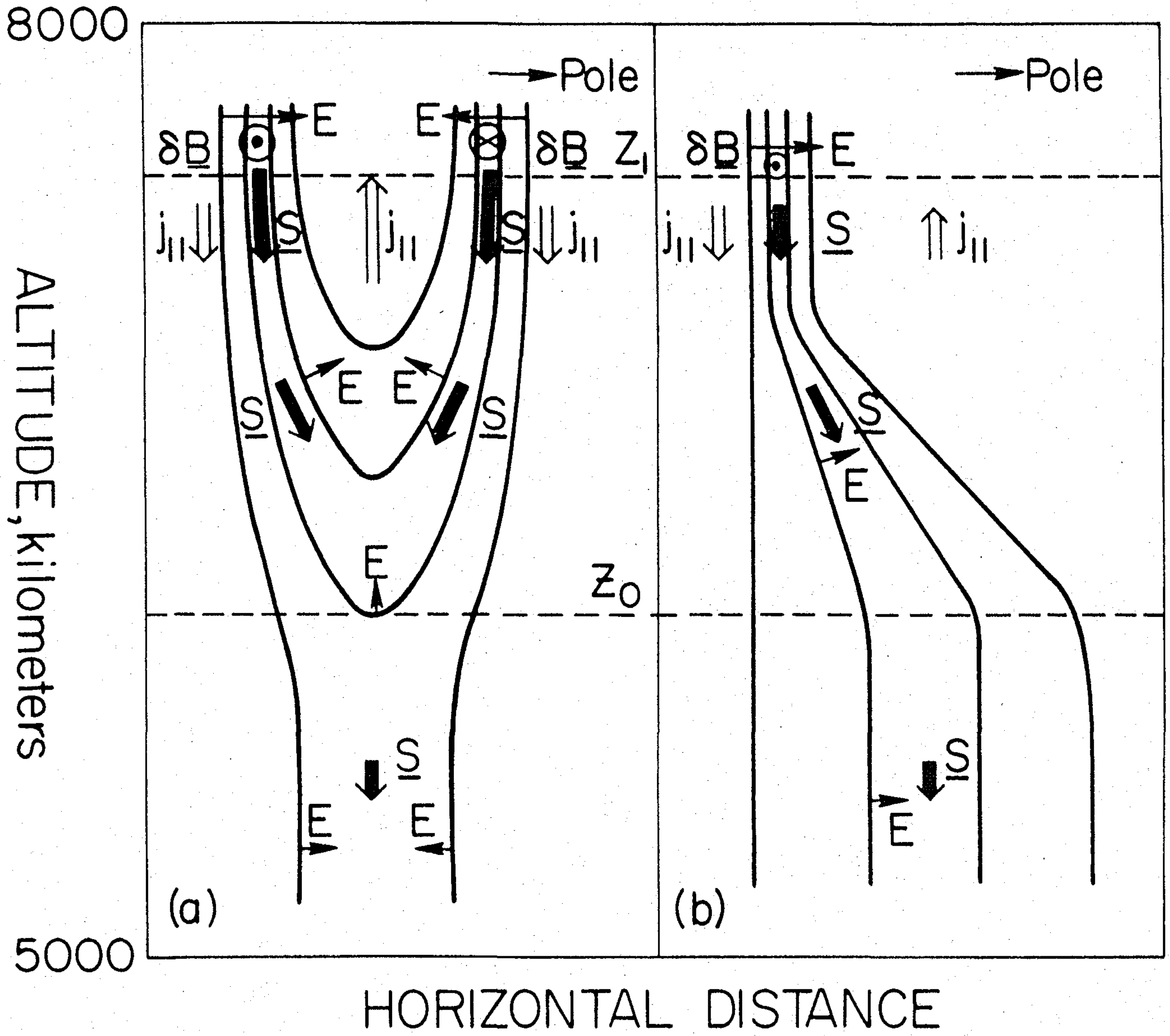

8000
5000
ALTITUDE, kilometers
HORIZONTAL DISTANCE
Pole
Pole
E
E
δB
δB
Z1
Z0
S
E
j∥
(a)
(b)

4

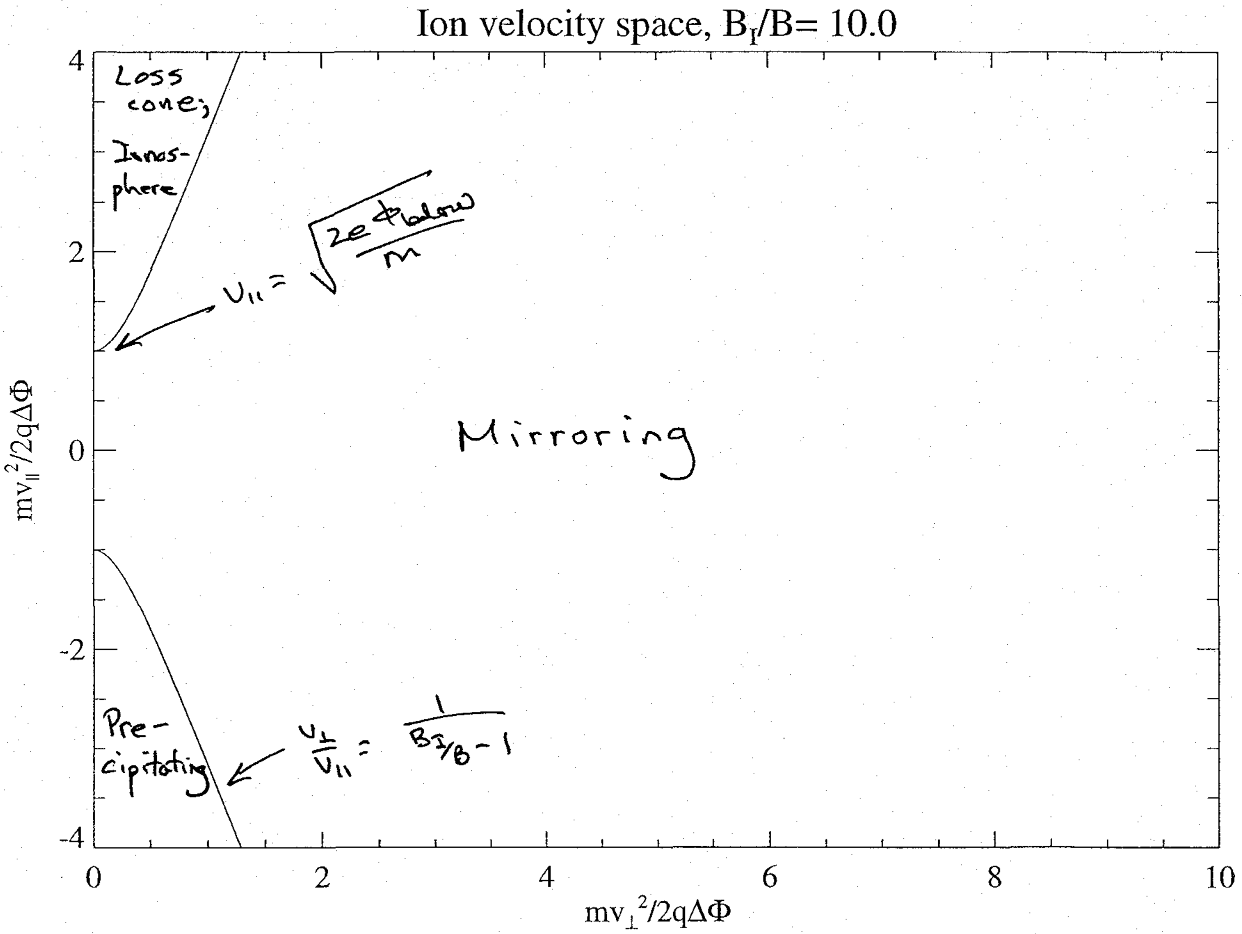
Ion velocity space, B_I/B= 10.0
Loss cone; Ionos-phere
$v_{\parallel} = \sqrt{\frac{2e\Phi_{below}}{m}}$
Mirroring
Pre-cipitating
$\frac{v_\perp}{v_\parallel} = \frac{1}{B_I/B - 1}$
$mv_{\parallel}^2/2q\Delta\Phi$
$mv_{\perp}^2/2q\Delta\Phi$

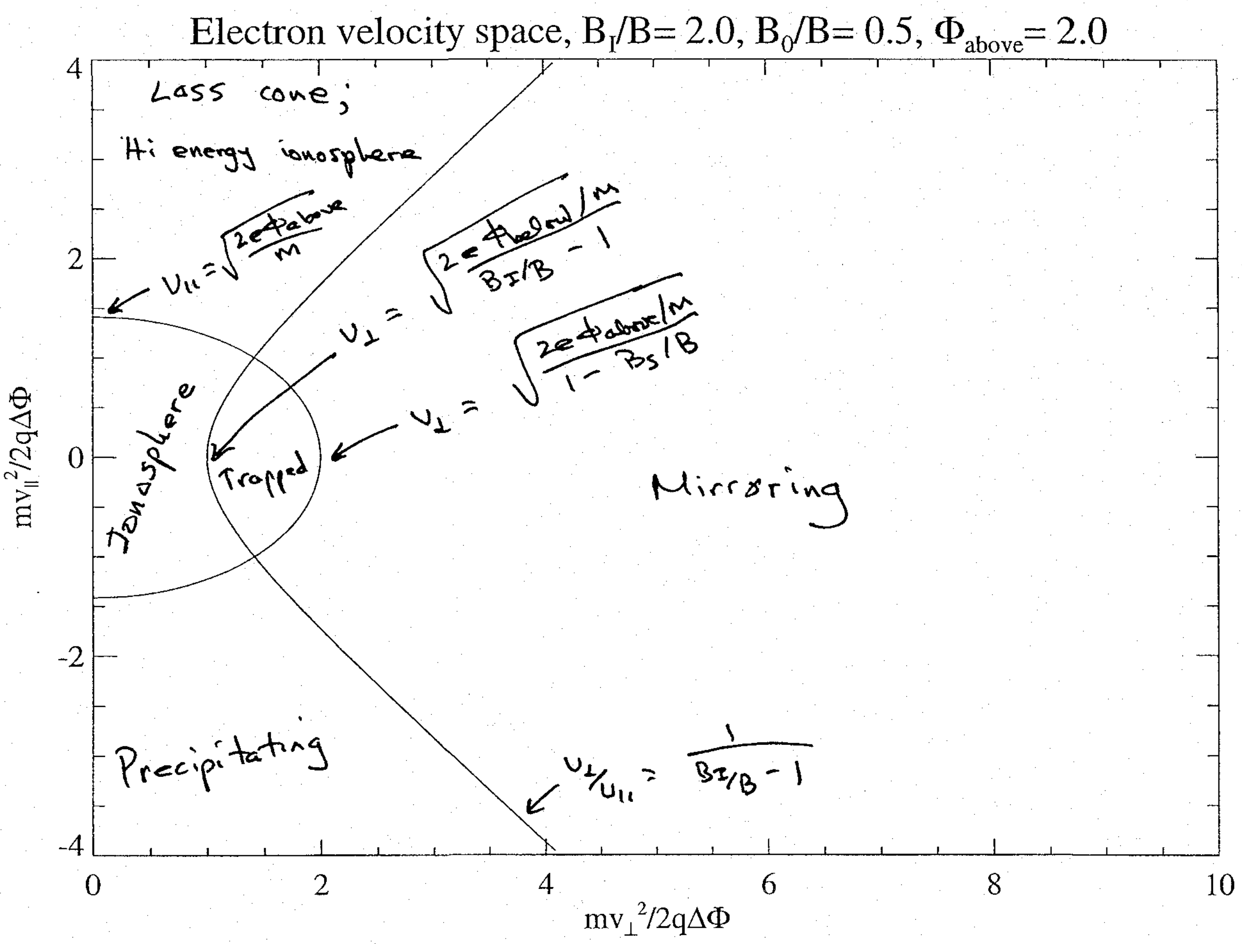

Electron velocity space, $B_I/B= 2.0$, $B_0/B= 0.5$, $\Phi_{above}= 2.0$
Loss cone;
Hi energy ionosphere
$v_{\parallel} = \sqrt{\frac{2e\Phi_{above}}{m}}$
$v_\perp = \sqrt{\frac{2e\Phi_{below}/m}{B_I/B - 1}}$
$v_\perp = \sqrt{\frac{2e\Phi_{above}/m}{1 - B_S/B}}$
Ionosphere
Trapped
Mirroring
Precipitating
$v_\perp/v_\parallel = \frac{1}{B_I/B - 1}$
$mv_\parallel^2/2q\Delta\Phi$
$mv_\perp^2/2q\Delta\Phi$

altitude of 240 km. As illustrated in Figure 1, the satellite spin axis is perpendicular to the orbit plane such that the spacecraft executes a cartwheel motion in its orbit plane with a spin period of about 18 s. The three orthogonal boom pairs and the six spherical sensors for the electric field experiment are illustrated in Figure 1, as

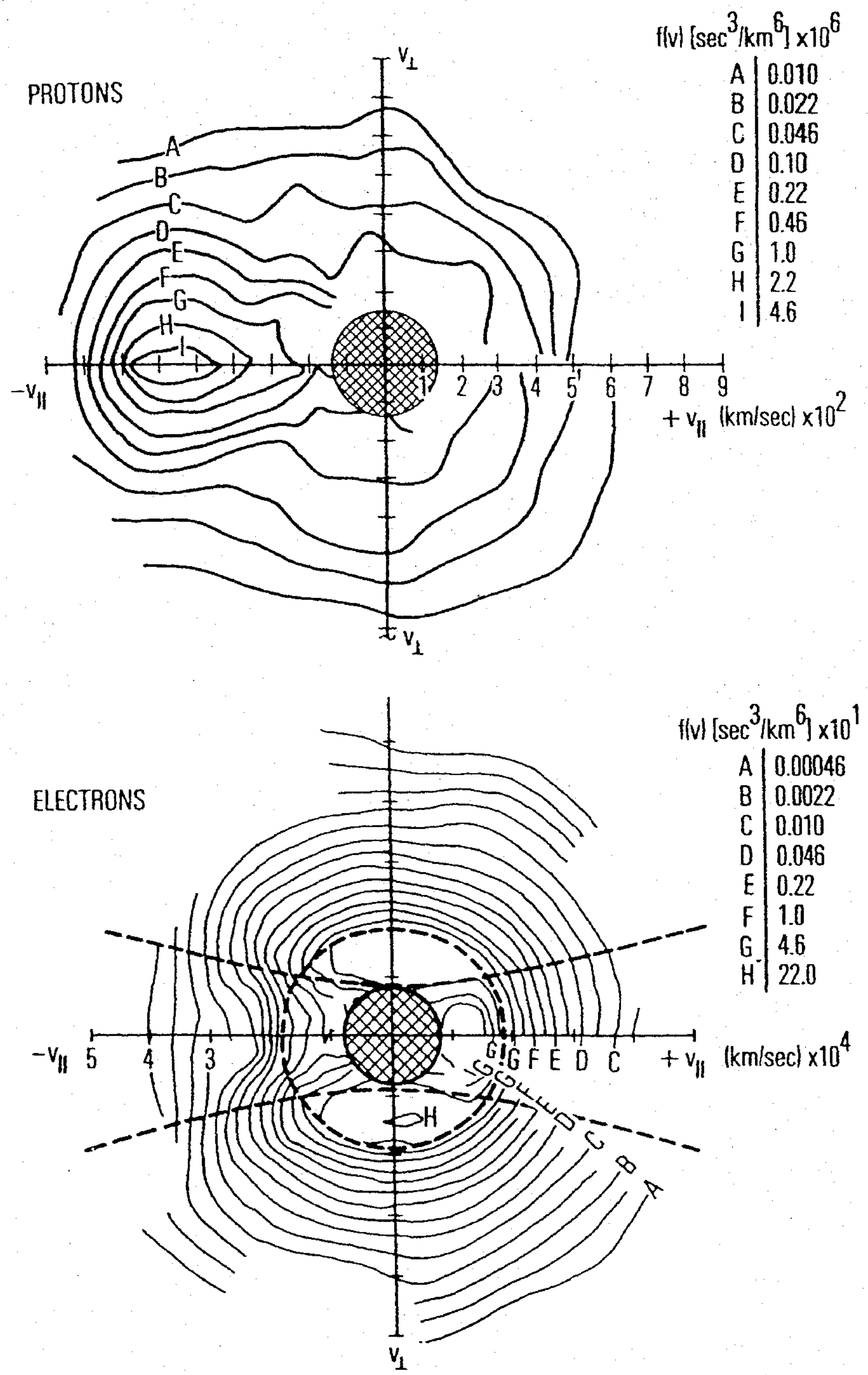

Fig. 2. Distribution contours of protons and electrons for UT = 12111 to 12129 on August 12, 1976.

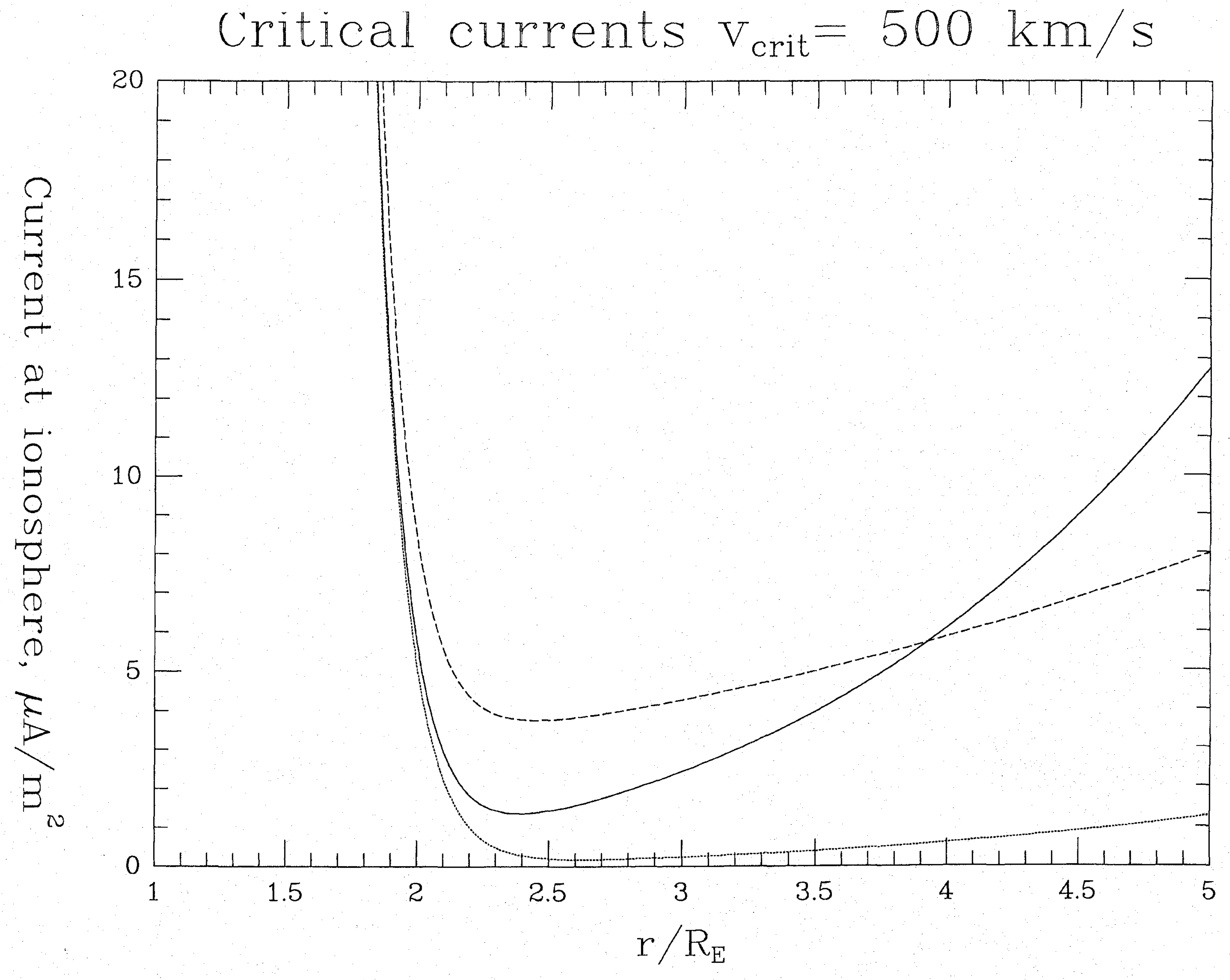
Critical currents v_{crit}= 500 km/s
Current at ionosphere, $\mu A/m^2$
20
15
10
5
0
1
1.5
2
2.5
3
3.5
4
4.5
5
r/R_E

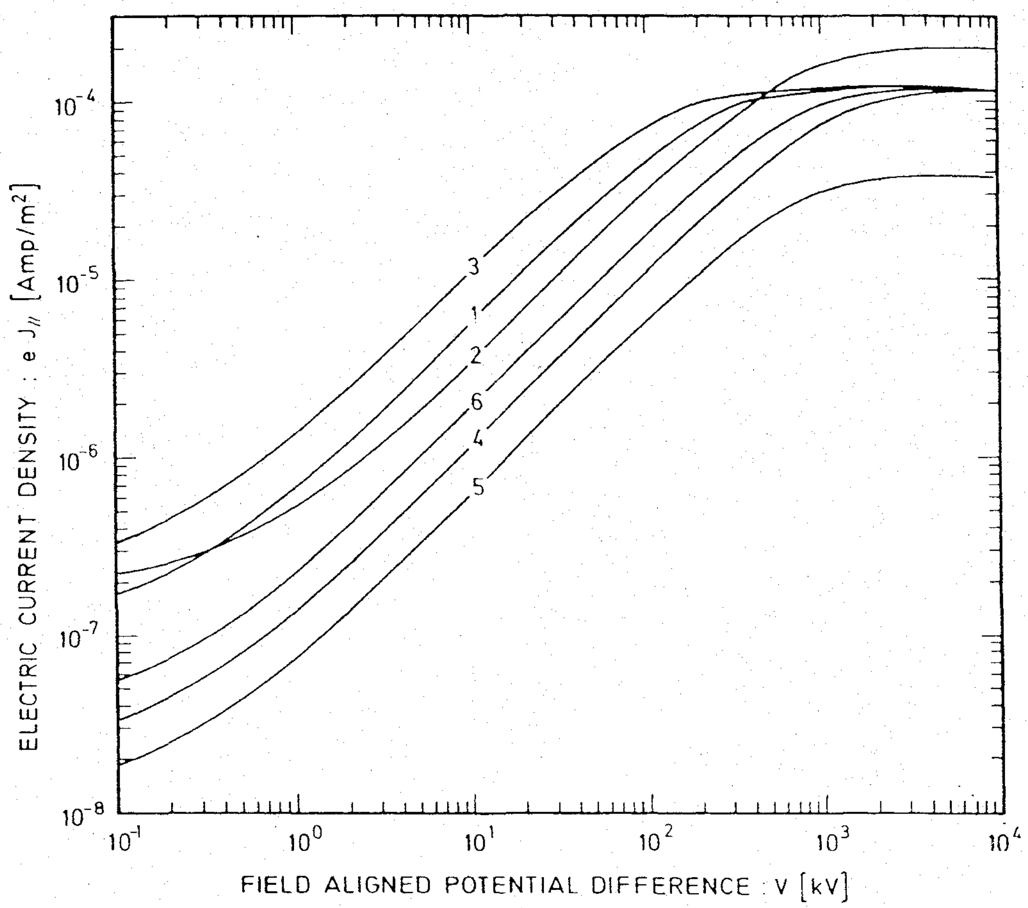

Fig. 3. Characteristic curves showing the field-aligned electric current density (in A/m^2) carried by the hot precipitating electrons as a function of the electric potential difference V (in kV) for six sets of plasma densities and temperatures (given in Table 1) in the source region at $L \cong 8$.

small compared to unity, unless the velocity distribution is ighly anisotropic (i.e., for $E_{0,\|}/E_{0,\perp} \gg B'/B^S \cong 1000$). For L : 8–10, $x \cong 0.001$–0.005. $J_\|$ and ε are nonlinear functions of ıe field-aligned potential difference V.

NUMERICAL RESULTS

Figure 3 shows the electric current density $eJ_\|$ (in A/m^2) as function of V for different values of N_e, $E_{0\|}$, $E_{0\perp}$, and B'/B^S iven in Table 1.

It can be seen that the current density carried by the precipitated electrons varies by several orders of magnitude when he potential V varies from 10^{-1} to 10^4 kV. Since the maxinum observed field-aligned current measured in auroral :vents does not in general exceed 10^{-5} A/m^2, one can con:lude that the field-aligned electric potential is generally beow 100 kV.

This current density is proportional to N_e, the density of hot :lectrons in the source region, and depends on the thermal ;pread ($E_{0\|}$) and on the pitch angle anisotropy ($E_{0\|}/E_{0\perp}$). There is a large range of V values for which the slope of the characteristic curves' ($eJ_\|$, V) is almost independent of V, i.e., fully neglected in these calculations, there is a don values for which convergent magnetic flux tubes l linear or ohmic conductors, whose resistance (or imp $= dV/dJ_\|e$) is then equal to $E_{0\perp}(2\pi m_e)^{1/2}/(E_{0\|}{}^{1/2}e^2N_e$ below).

For $V < 1\ kV$ and $V > 100\ kV$ the field-aligned s comes a nonlinear conductor (nonohmic-like condu impedance is always positive for any value of V. large values of the applied potential difference, Z te finity and $J_\|$ tends asymptotically to a maximum va ration plateau) which is equal to $(B'/B^S)N_e(E_{0\|}/2\pi m$

The 'characteristic curves' shown in Figure 3 are the curve given in Figure 1 of the article by *Lemaire rer* [1974]. Note, however, that in the present pape sider only the partial electric current carried by the l itating electrons, while in the latter reference the au considered the total electric current, including the p rents carried by other electric charges (i.e., the pr hot protons, the escaping cold electrons and ions o sphere) which also are present in the physical syste 'cept for very small field-aligned potential difference

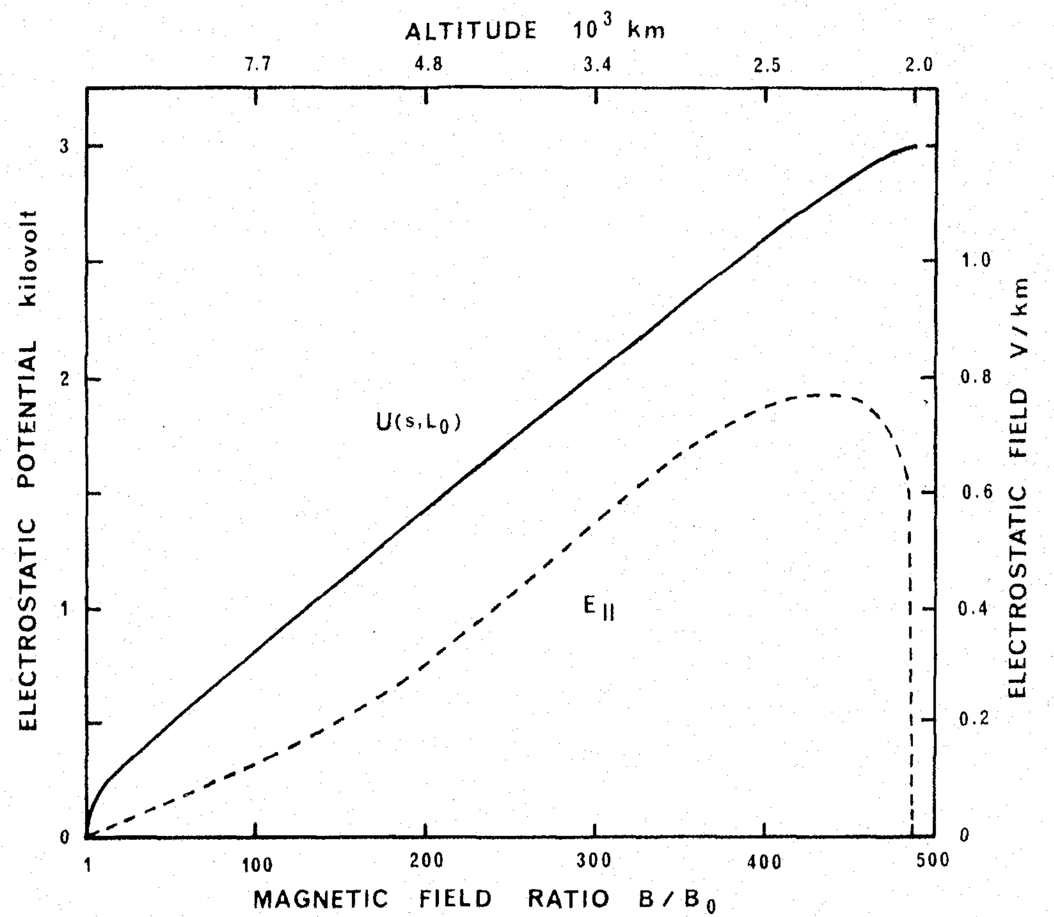

Fig. 3. Self-consistent solution for the structures of the electrostatic potential U and parallel electric field $E_\parallel$ at the center of the arc L_0.

The perpendicular electric field is

$$\mathbf{E}_\perp = \frac{\hat{\nu}}{h_\nu} R_E (L/L_0)^2 (\tilde{L}L_0)^{1/2} (1 + C_Q)\varphi(s) \sin\left[\frac{L - L_0}{L_0} (\tilde{L}/L_0)^{1/2}\right] \tag{56}$$

Thus the value of $E_\perp$ at the ionosphere determines $\varphi(l)$. Since the potential drop along the center field line $\phi_l = \varphi(0) - \varphi(l)$ is determined from particle data, the potential normalization

electron energy flux data observed at 7300 km over the northern auroral region for different pitch angles by the S3-3 satellite on August 12, 1976. Figure 2 shows electron energy flux data for essentially the same event observed at 275 km over the southern auroral region by the same satellite. The solid (0° pitch angle) and dashed (180° pitch angle) curves show a fit of the low-altitude data set with our model distribution functions, assuming that there is a total potential drop of 3 kV between the equator and the baropause at $L_0 = 8.35$ (invariant

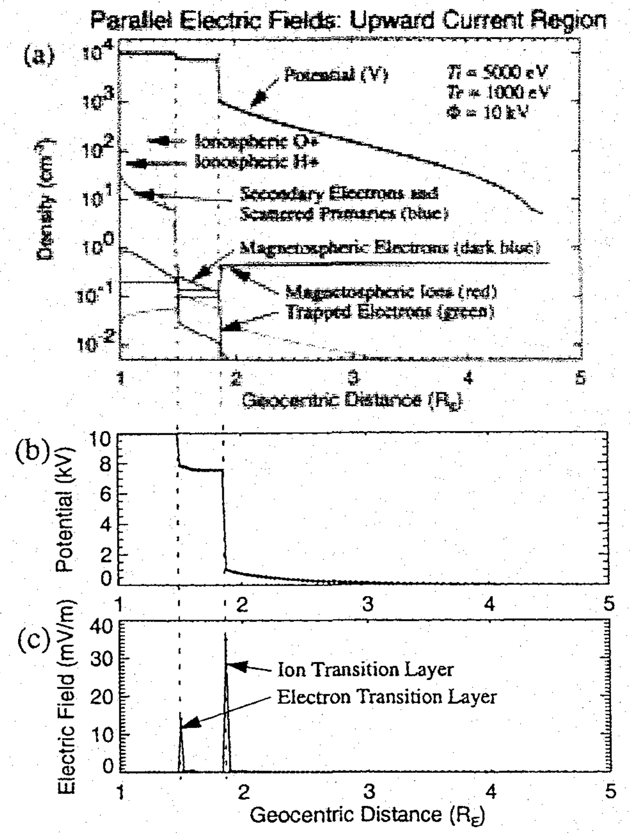

Figure 2. The results of a 1-D spatial, 2-D velocity large-scale Vlasov simulation. (a) Ionospheric O^+ (orange), ionospheric H^+ (yellow), electron secondaries and scattered primaries (blue), and cold electron distributions are specified at the left boundary. The plasma sheet electrons (dark blue) and ions (red) are specified at the left boundary. The trapped regions are filled in with the same phase space density as the magnetospheric electrons as a function of energy, up to a value of $\alpha^* f_{max}$, where $\alpha = 0.02$. The circles represent the potential (Φ). (b) Φ on a linear scale. (c) The one pixel averaged electric field on a linear scale.

field component perpendicular to the ambient magnetic field (***B***) and nearly along the spacecraft velocity vector. The large positive excursions (~21:02:00 UT) followed by a large negative excursion (~21:02:14 UT) are indicative of a converging electric field structure which implies a parallel electric field.

Panel (c) displays the electron energy flux as a function of energy (vertical axis). Panel (d) displays the ion energy flux in the same format. From the left hand side of the plot until ~21:02:15 UT, there are downward accelerated electrons and an up-going ion beam. We conclude that there is a parallel electric field both above and below the spacecraft.

Panel (b) displays the plasma density using two different techniques. The red trace is the density derived from the electron distributions using >100 eV particles; the circles are the density derived from wave dispersion. The agreement of the quantities implies that the plasma sheet electrons dominate the auroral cavity and, notably, that there is little or no cold electron population [*Strangeway et al.*, 1998; *Ergun et al.*, 1998b; *McFadden et al.*, 1999].

After ~21:02:14 UT, the spacecraft was below the auroral cavity and therefore in a region dominated by ionospheric plasma. The electron fluxes below ~5 keV dramatically increase. The hot (>100 eV) electron density increases, but not as dramatically as the total density inferred from the wave dispersion implying a substantial cold (< 100 eV) electron population.

Table 1. Boundary Conditions

Species	Density	Temperature	Type of Distribution	Boundary
Ionospheric O^+	2×10^5 cm^{-3}	0.5 eV	Fluid	Left
Ionospheric H^+	100 cm^{-3}	0.5 eV	Fluid	Left
Secondaries (e^-)	30 cm^{-3}	~100 eV	Power Law: $f \sim v^{-5.25}$	Left
Scattered Primaries	1 cm-3	~1 keV	Fit to data.	Left
Ionospheric e^-	2×10^5 cm^{-3}	0.5 eV	Boltzman Fluid	Left
Magnetospheric H^+	0.5 cm^{-3}	5 keV	Maxwellian	Right
Magnetospheric e^-	0.5 cm^{-3}	1 keV	Maxwellian	Right
Trapped e^-	$\alpha = 0.02$		Filled Maxwellian	

III. Numerical Simulations

A static, 1-D spatial, 2-D velocity, Vlasov code was used to search for large-scale, self-constant solutions of the parallel electric

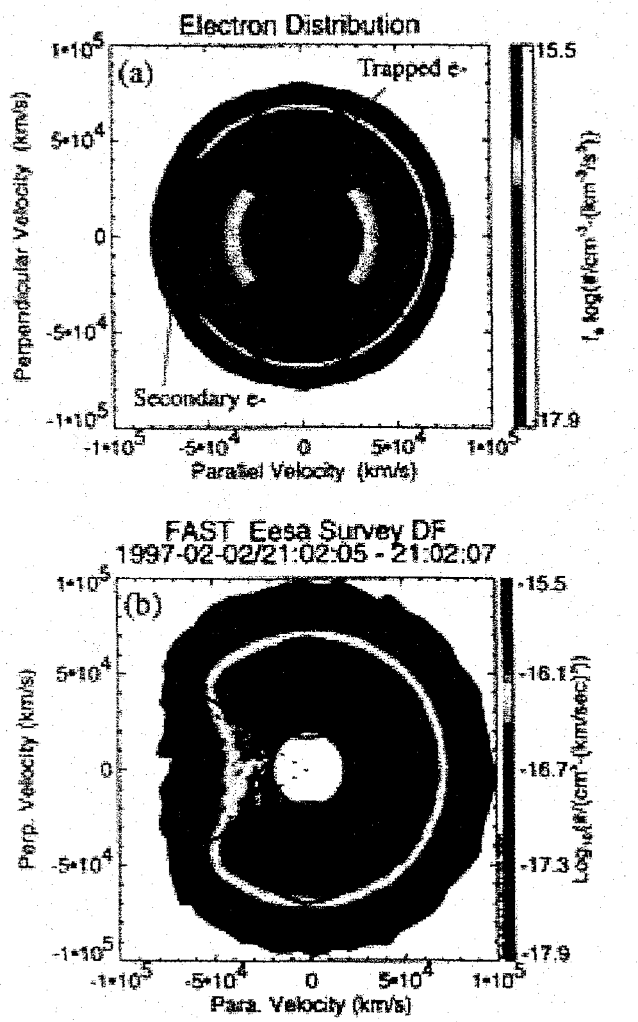

Figure 3. (a) The electron distribution from the adiabatic simulation. The boundaries between the magnetospheric, secondary and scattered primary, and trapped electrons are marked with solid lines. (b) An electron distribution in the auroral cavity in Figure 1 as measured by FAST. The dashed lines are the loss cone with no electric field. The distributions are quantitatively similar except in the region of secondary and scattered primary electrons. Velocity space diffusion may account for the differences between the distributions.

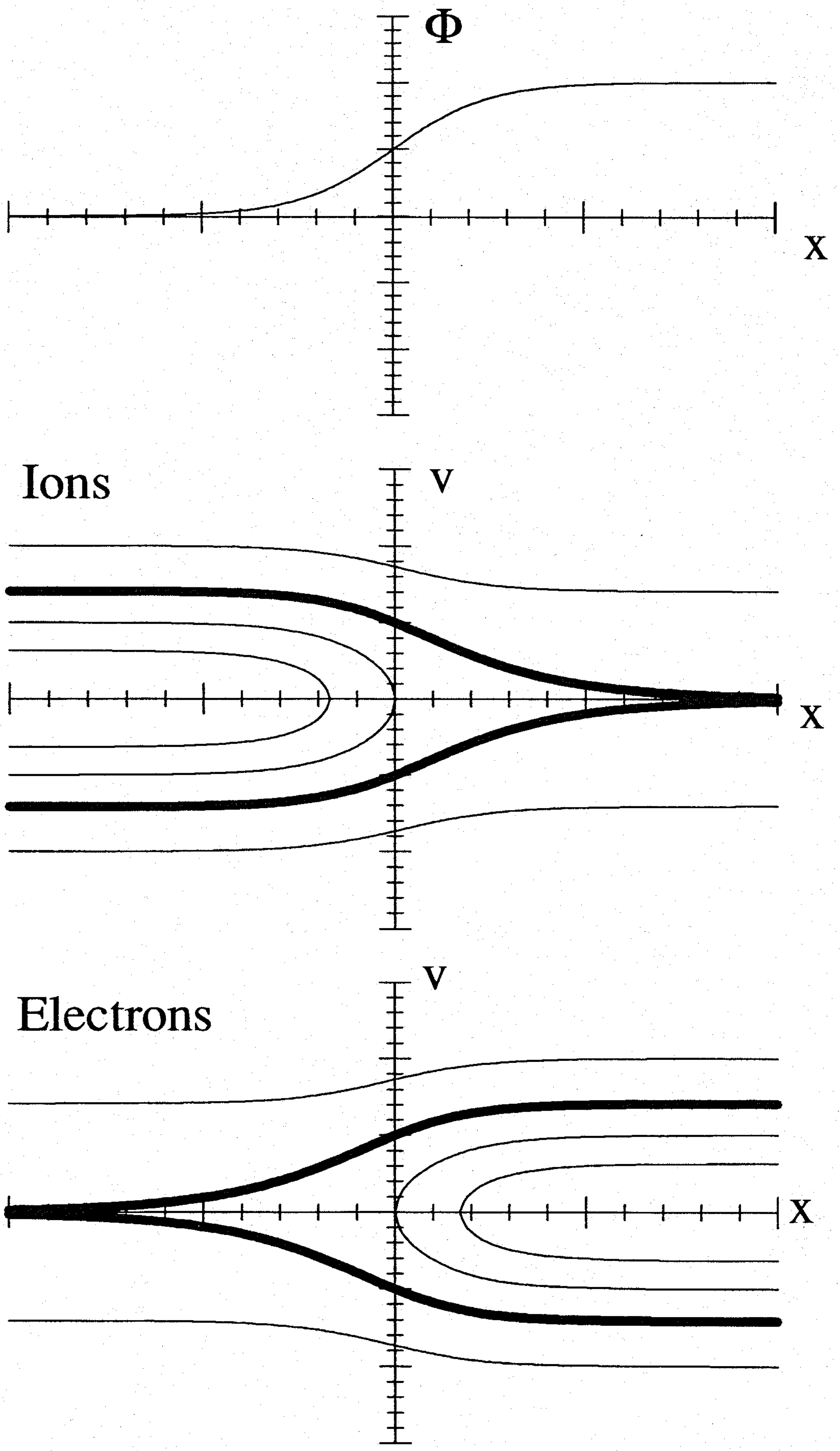
Φ
x
Ions
v
x
Electrons
v
x

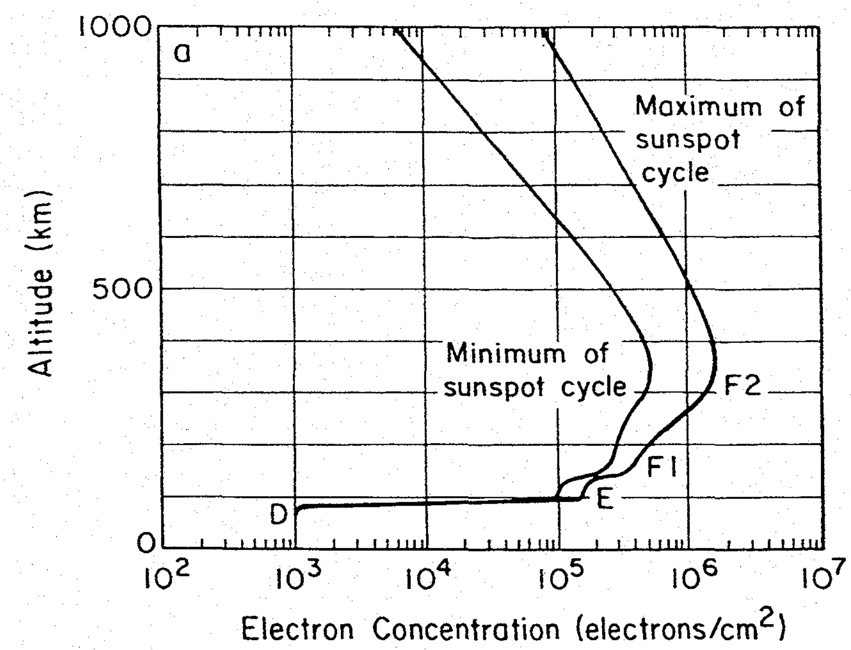

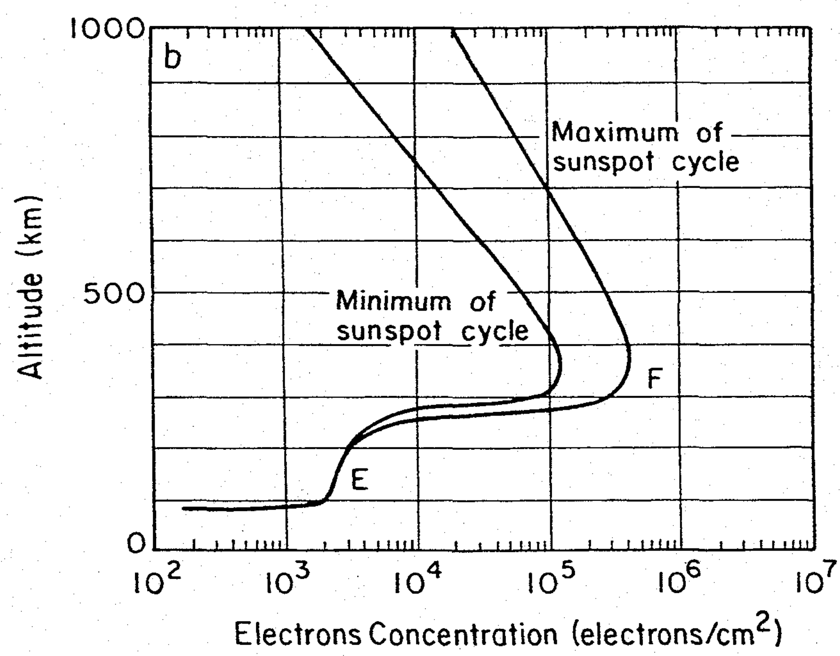

Fig. B.1. Typical mid-latitude distributions at the extremes of the sunspot cycle for daytime (a) and nighttime (b) conditions. [From Johnson (1961).]

The first derived quantity is the ion collision frequency (Chapman, 1956), given by

$$\nu_{in} = (2.6 \times 10^{-9})(n_n + n_i)A^{-1/2} \quad s^{-1}$$

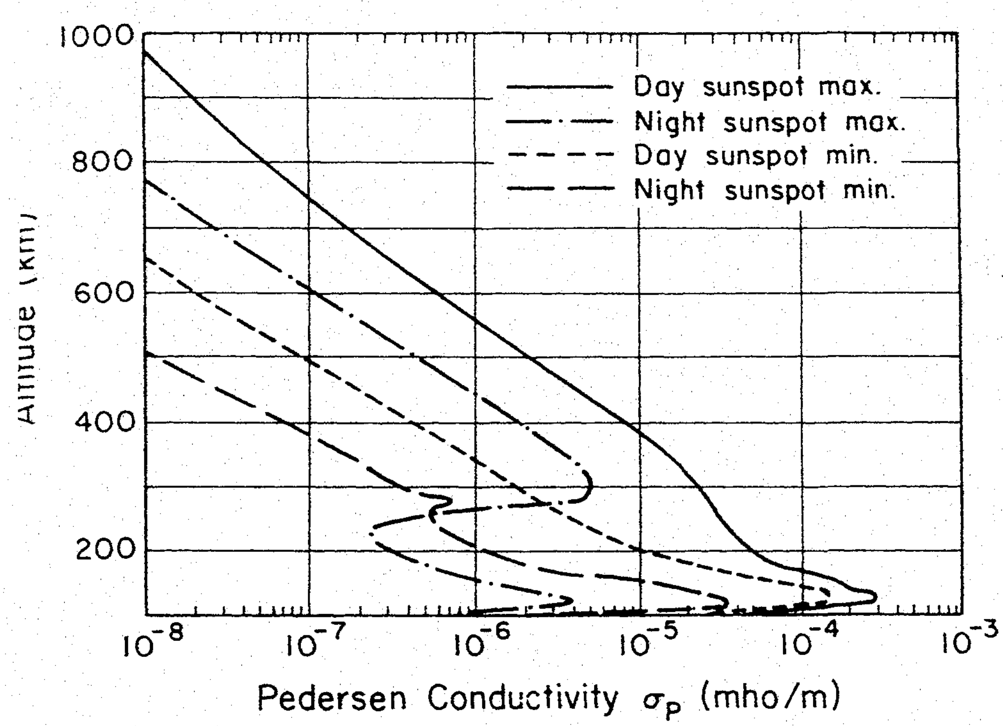

Fig. B.5. Pedersen conductivity versus altitude. [From Johnson (1961).]

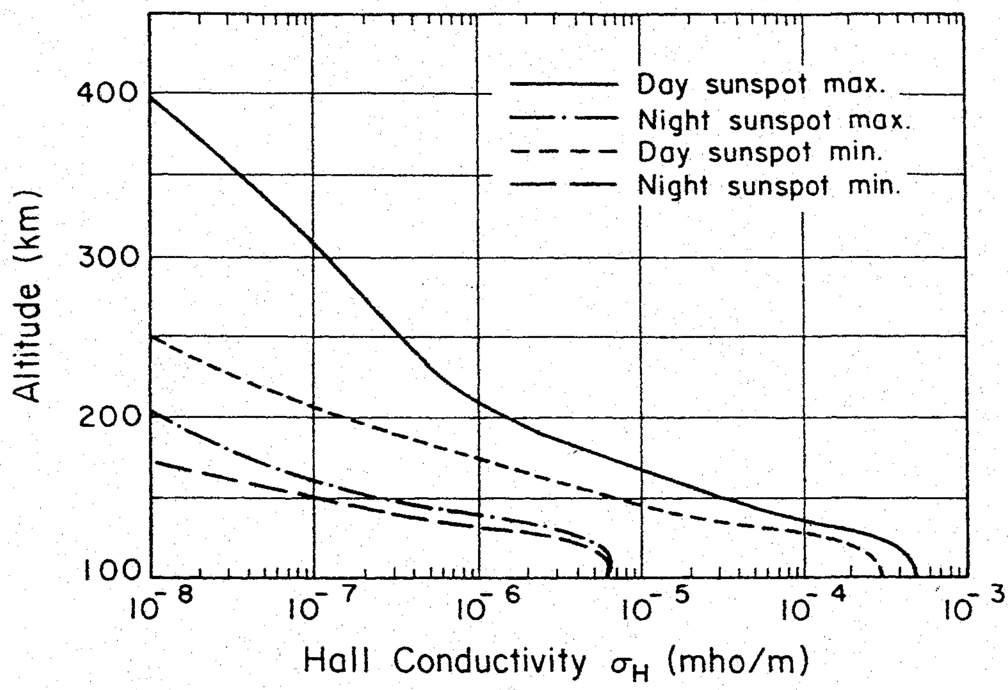

Fig. B.6. Hall conductivity versus altitude. [From Johnson (1961).]

iscellaneous Formulas

expressions B is in gauss, n is in reciprocal cubic centimeters, R_e =
ı = one earth radius, temperature is expressed in electron volts, electric

MHD Wave Modes

Linearized MHD equations give three waves ($\beta \equiv 8\pi p / B^2 \ll 1$):

- Slow mode (ion acoustic wave): $\omega = k_{\parallel} c_s \quad (c_s = \sqrt{\gamma p / \rho})$

  Electron pressure coupled to ion inertia by electric field.

  Balances pressure parallel to magnetic field.

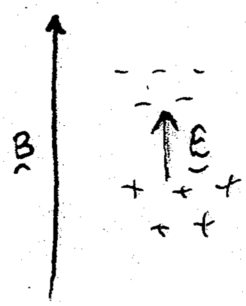

- Intermediate mode (Alfvén wave): $\omega = k_{\parallel} V_A \; (V_A = \sqrt{B^2 / 4\pi\rho})$

  Magnetic tension balanced by ion inertia.

  Carries field-aligned current along magnetic field.

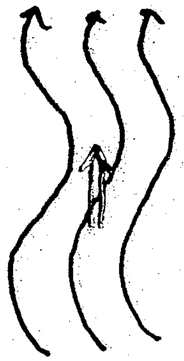

- Fast mode (magnetosonic wave): $\omega = \sqrt{k^2 V_A^2 + k_{\perp}^2 c_s^2}$

  Magnetic and plasma pressure balanced by ion inertia.

  Balances pressure across magnetic field.

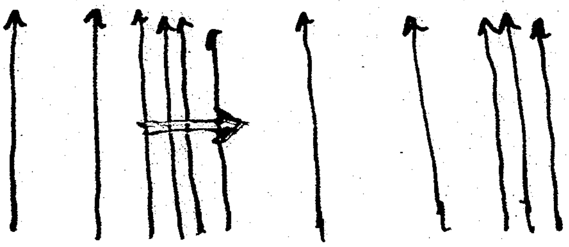

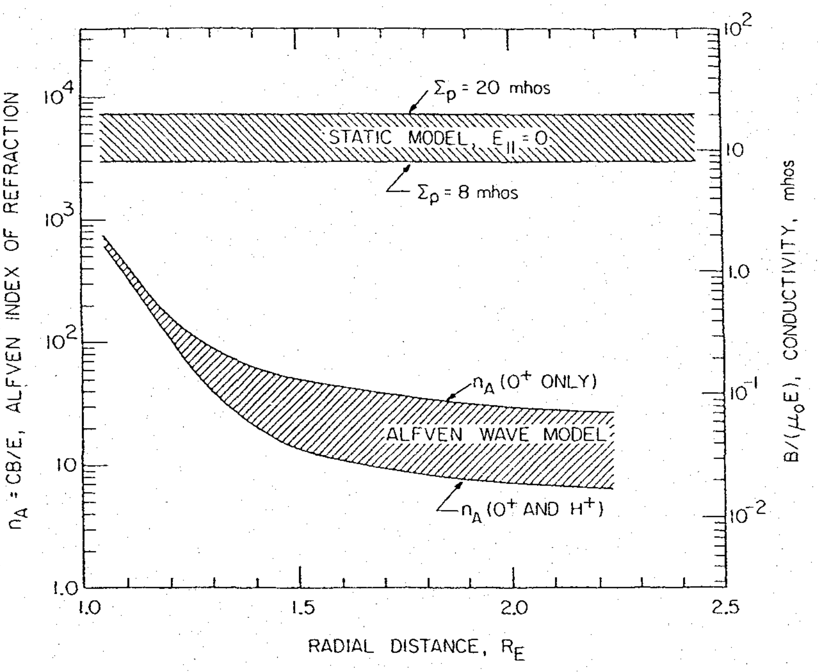

Fig. 14. A model of the Pedersen conductivity and the Alfven index of refraction as a function of radial distance for comparison with Figure 10. The electron density profile used in this model for n_A is taken from *Persoon et al.* [1983]. The upper limit on n_A assumes that the plasma is entirely O^+, and the lower limit assumes a transition from H^+ to O^+ at about 1.4 R_E. The limits on Σ_P are from *Horwitz et al.* [1978].

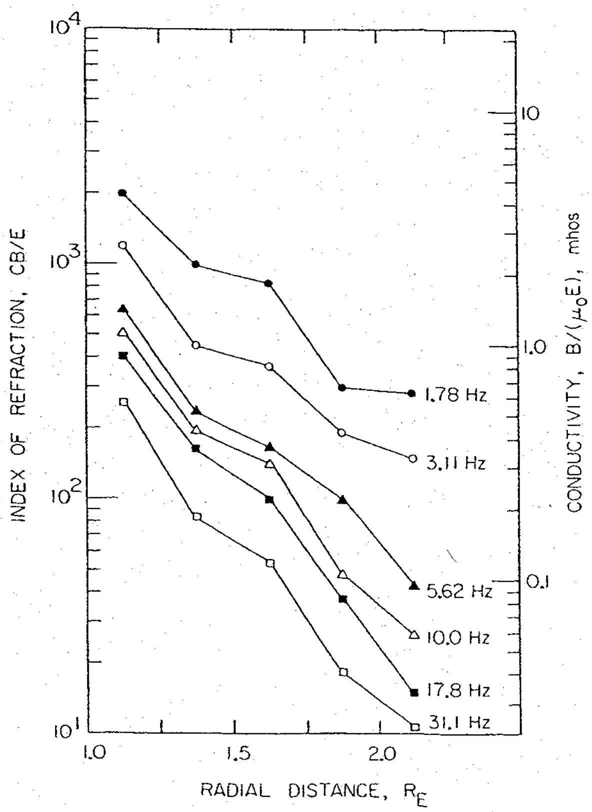

Fig. 10. A plot of the average magnetic to electric field ratio all events studies expressed as a function of altitude. Note the strc tendency for the magnetic to electric field ratio to decrease with creasing radial distance and also with increasing frequency.

restricted to the polar cap, comparisons in specific cases show that the density in the auroral regions is usually only slightly lower than the polar cap densities. Using the density profile obtained by *Persoon et al.* [1983] at high altitudes and the densities measured by *Chan and Colin* [1969] at low altitudes, the model shown in Figure 14 has been constructed. The shaded region marked "Alfven wave model" indicates the estimated range of n_A values. The wide range of uncertainty at high altitudes is due to the unknown plasma composition and scale height at high altitudes. The upper limit assumes that the plasma is entirely O^+, and the lower limit assumes a transition form O^+ to H^+ at about 1.4 R_E. Because this is an "average" model, significant deviations can be expected because of seasonal effects, auroral activity, and other factors, particularly at high altitudes.

Comparing the measured cB/E ratios in Figure 10 with the model for the radial variation of the Alfven index of refraction in Figure 14, it can be seen that both cB/E and n_A decrease rapidly with increasing radial distance. Usually, the measured cB/E ratios lie somewhat above n_A. This tendency can be verified in specific cases. For example, in Figure 7 a typical auroral electron density at $R = 1.22$ R_E is $n_e \simeq 10^3$ cm^{-3} [*Chan and Colin*, 1969], which gives $n_A = 54$. The top panel of Figure 7 shows that the measured cB/E ratios are about a factor of 10 larger than the n_A values given by the model. Similarly, in Figure 8 a typical auroral electron density at $R = 1.10$ R_E is $n_e \simeq 10^5$ cm^{-3} [*Chan and Colin*, 1969], which gives $n_A = 325$. The measured cB/E ratios in this case are about a factor of 5 larger than the n_A values given by the model. Typically, the magnetic to electric field ratio is about a factor of 2 to 10 above the value determined by the Alfven index of refraction but always well below the value determined by the Pedersen conductivity. This result is consistent with the expectation of an Alfven wave model. As discussed by *Goertz and Boswell* [1979] and others, the magnetic to electric field

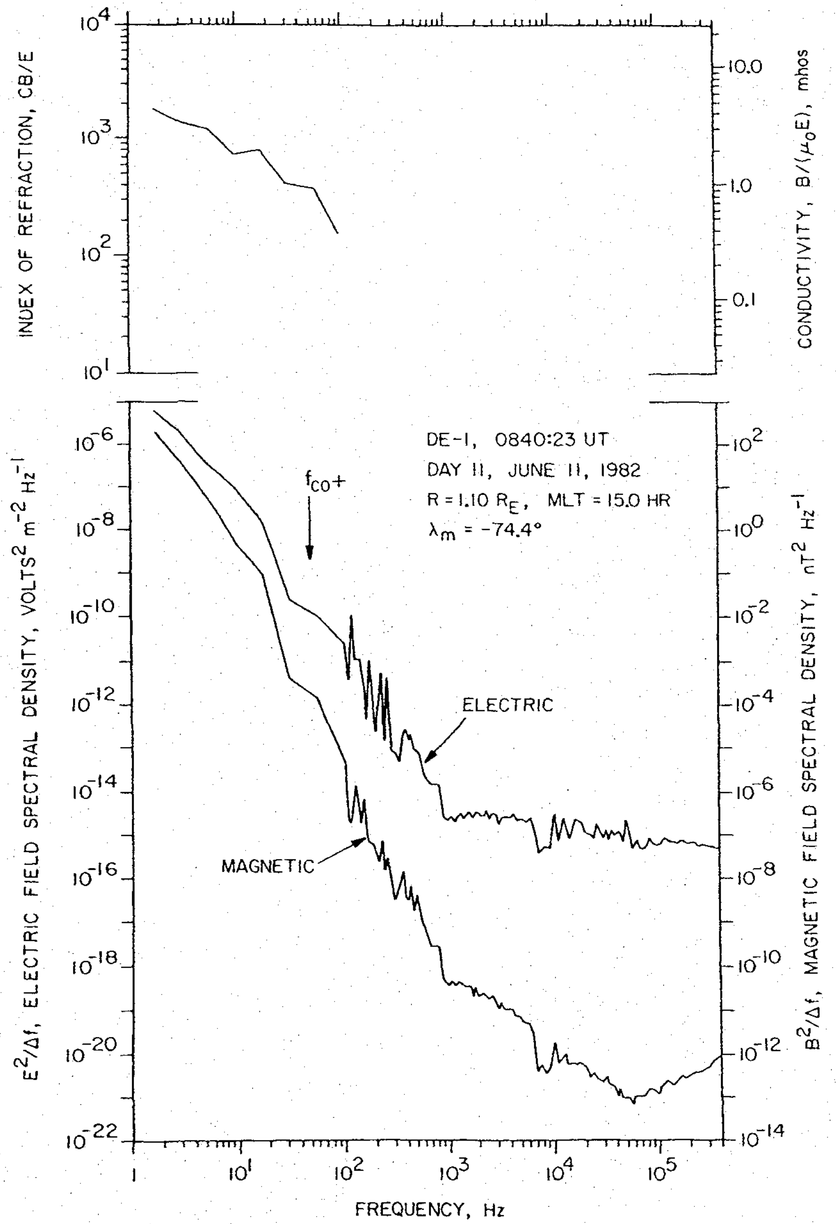

Fig. 8. Another set of spectrums comparable to Figure 7. Note that the magnetic spectrum has a distinct drop in intensity slightly below the O^+ cyclotron frequency, f_{cO^+}.

short time scales, the polarization is essentially random on a time scale comparable to the spacecraft rotation period. Other cases investigated show the same result. Therefore, it must be concluded that the polarization of the perpendicular component of the electric field is essentially random. No evidence is found for a consistent right- or left-hand polarization with respect to the earth's magnetic field. Polarization measurements could not be performed on the magnetic field because only one magnetic sensor is available for magnetic field measurements.

5. Possible Interpretations

Several interpretations can be advanced to explain the origin of the electric and magnetic noise observed along the auroral field lines. These interpretations can be classified as either a static model or an Alfven wave model. These models can be further subclassified on the basis of whether the electric field component parallel to the static magnetic field is assumed to be zero ($E_{\parallel} = 0$) or nonzero ($E_{\parallel} \neq 0$). We now consider these various interpretations in detail.

5.1. *Static Model ($E_{\parallel} = 0$)*

In the static model the noise is attributed to the motion of the spacecraft through static electric and magnetic field structures in the ionosphere. The frequency spectrum is then determined entirely by the Doppler shift, $\omega \doteq \mathbf{k}\cdot\mathbf{v}$. In this interpretation the possible association of features in the spectrum with the O^+ cyclotron frequency would have to be completely coincidental, because the Doppler shift bears no relationship to the cyclotron frequency. At a typical spacecraft velocity of about 10 km/s a Doppler shift of 50 Hz requires spatial scale lengths of about 200 m. This length scale is small, but not unreasonably small for auroral phenomena. Auroral arcs with thicknesses of only a few hundred meters have been reported [*Akasofu*, 1965].

Because of the high conductivity along the magnetic field

These differences may now be compared with results obtained experimentally.

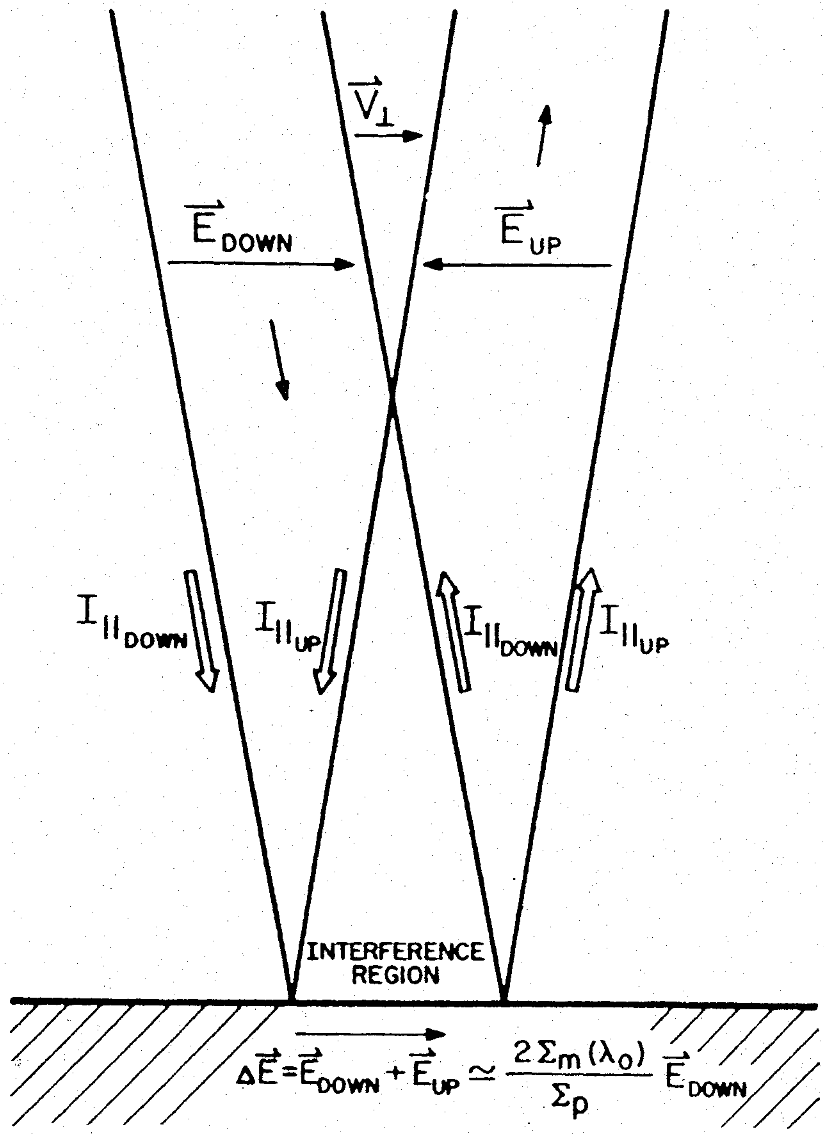

Fig. 5. Cross-sectional schematic of currents and fields in the vicinity of the ionosphere due to a magnetospheric source. The features are time independent in the frame of the arc. The reflected wave has slightly less than opposite the magnitude of the incident wave and returns along a path slightly 'down-stream' from the incident path owing to plasma convection. The boundary conditions yield small electric fields and large currents within the ionosphere which may be considered to be the result of interference between the incident and reflected waves. Above the ionosphere a pair of large-magnitude oppositely directed electric fields is observed.

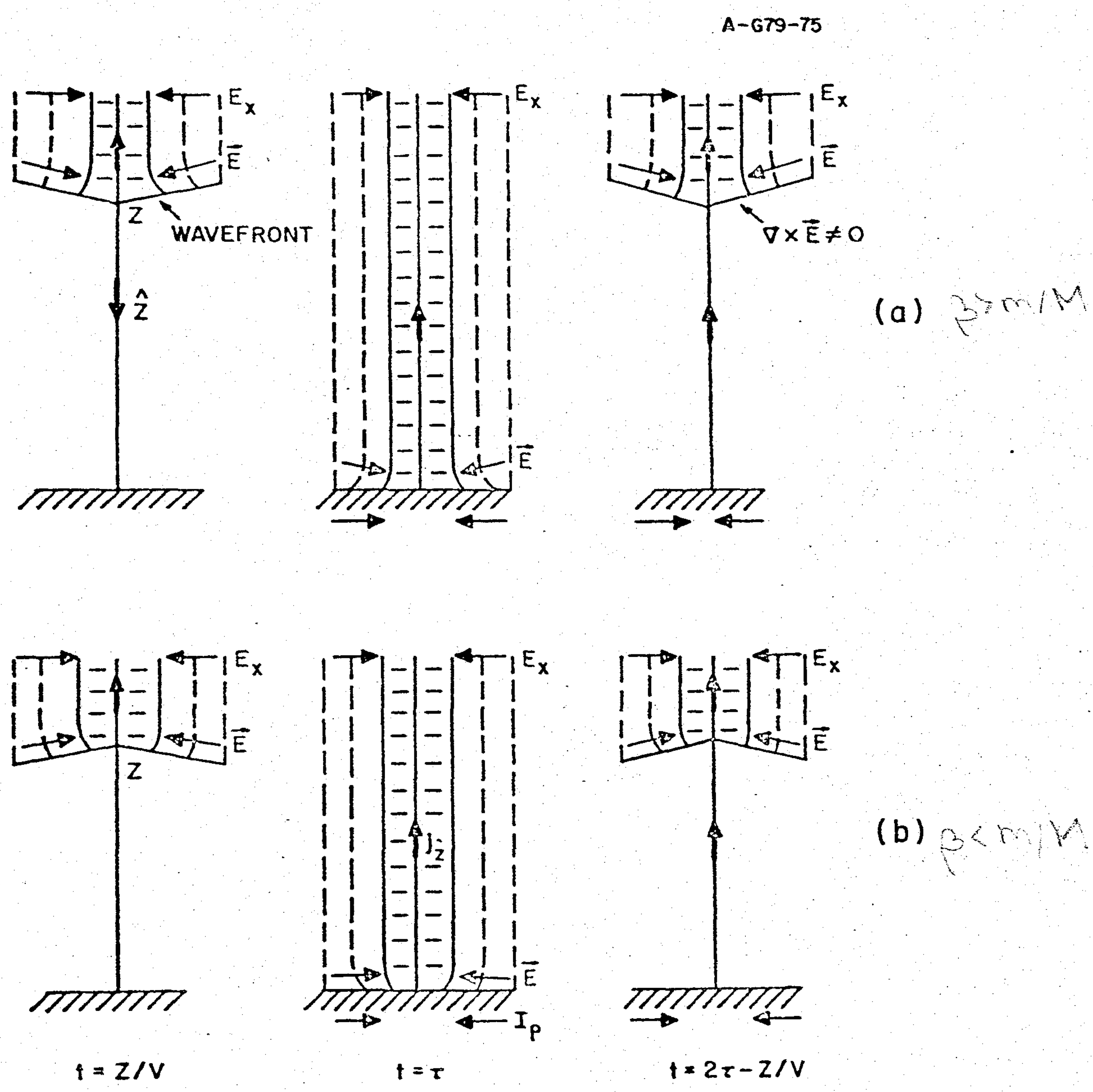
A-G79-75
E_x
$\vec{E}$
Z
WAVEFRONT
$\hat{Z}$
$\nabla \times \vec{E} \neq 0$
(a) β>m/M
(b) β<m/M
j_z
I_p
t = Z/V
t = τ
t = 2τ − Z/V

Figure 4

Freja satellite observations of E/B ratio in inertial limit (alt ~ 1700 km)

$$\frac{\delta E}{\delta B} = V_A \sqrt{1 + \left(\frac{2\pi\lambda_e}{\lambda}\right)^2}$$

$$\lambda_e = \frac{c}{\omega_{pe}}$$

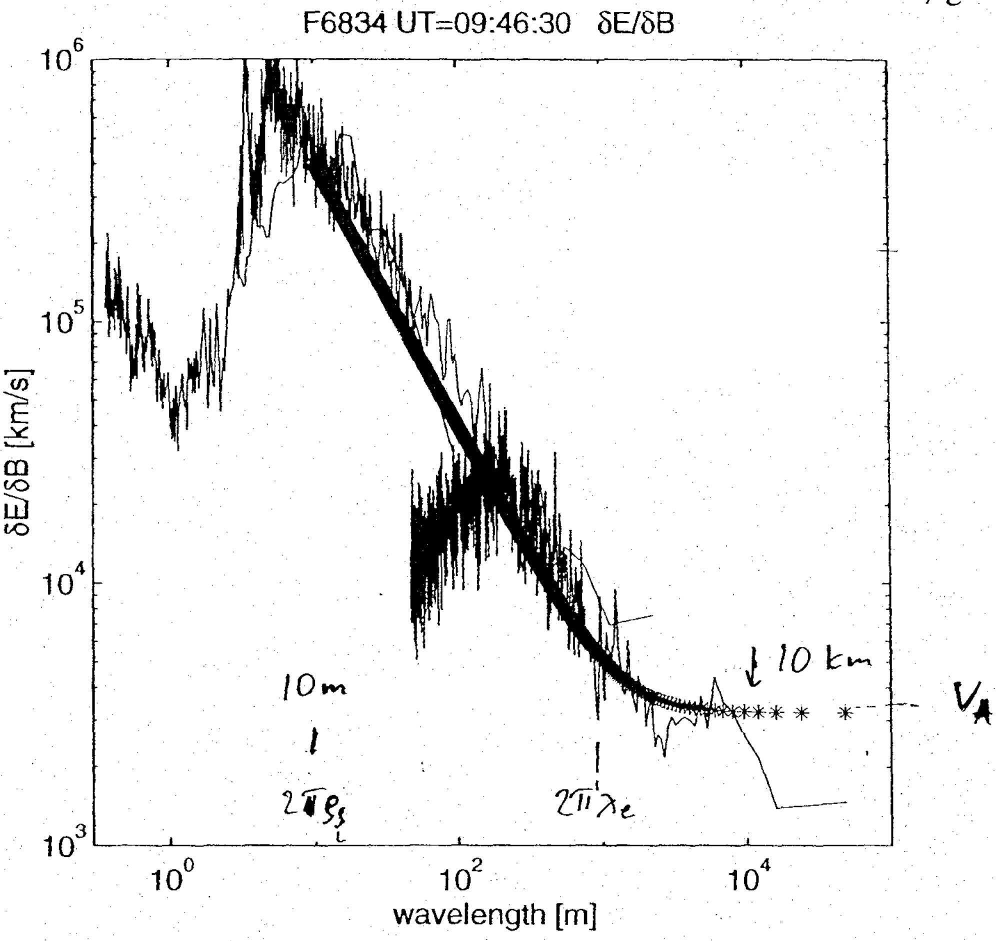

(Stasiewicz et al, 2000)

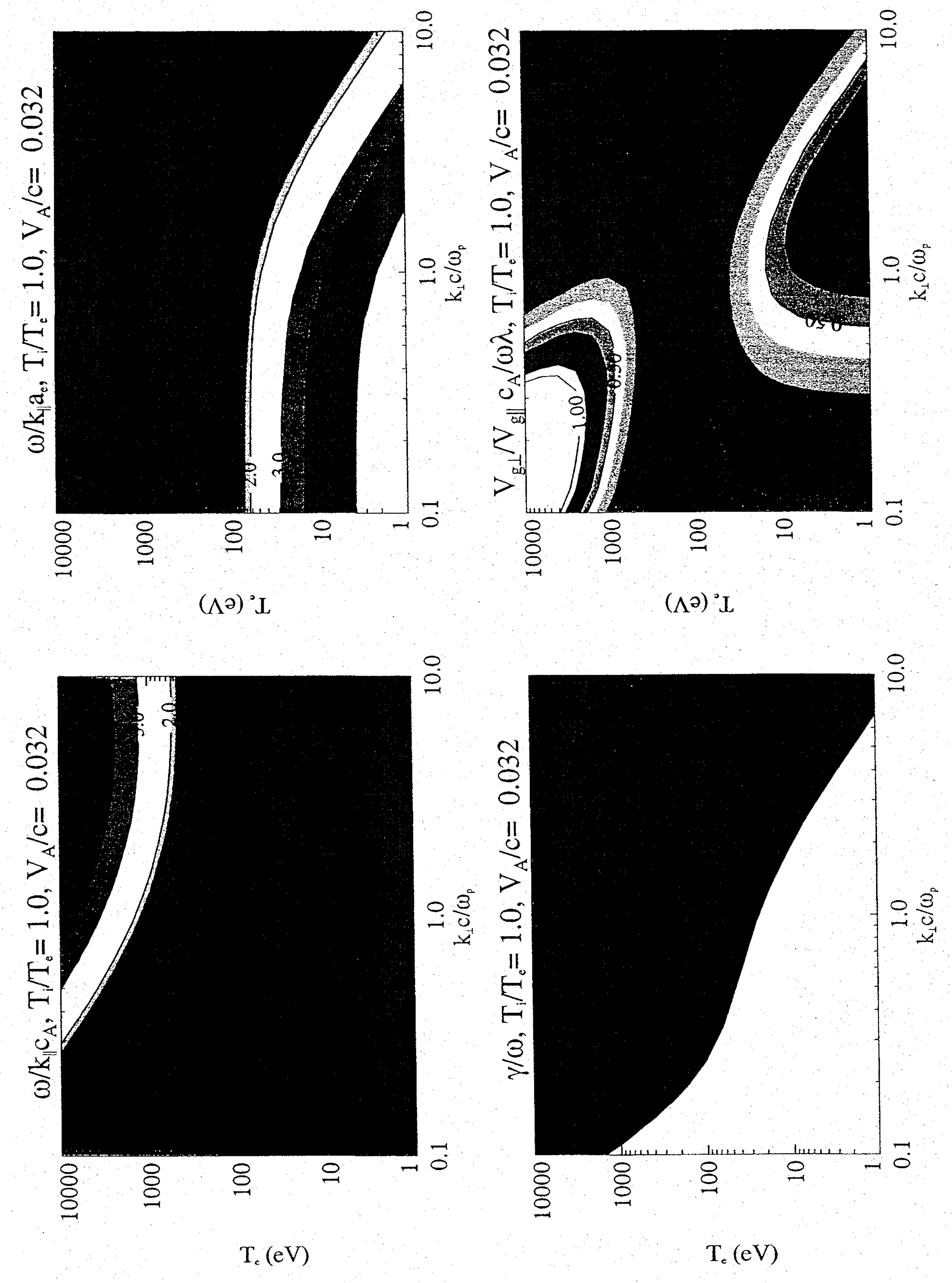
ω/k∥c_A, T_i/T_e= 1.0, V_A/c= 0.032
ω/k∥a_e, T_i/T_e= 1.0, V_A/c= 0.032
γ/ω, T_i/T_e= 1.0, V_A/c= 0.032
V_g⊥/V_g∥ c_A/ωλ, T_i/T_e= 1.0, V_A/c= 0.032
T_e (eV)
k⊥c/ω_p
10000
1000
100
10
1
0.1
1.0
10.0
2.0
3.0
1.00
0.50

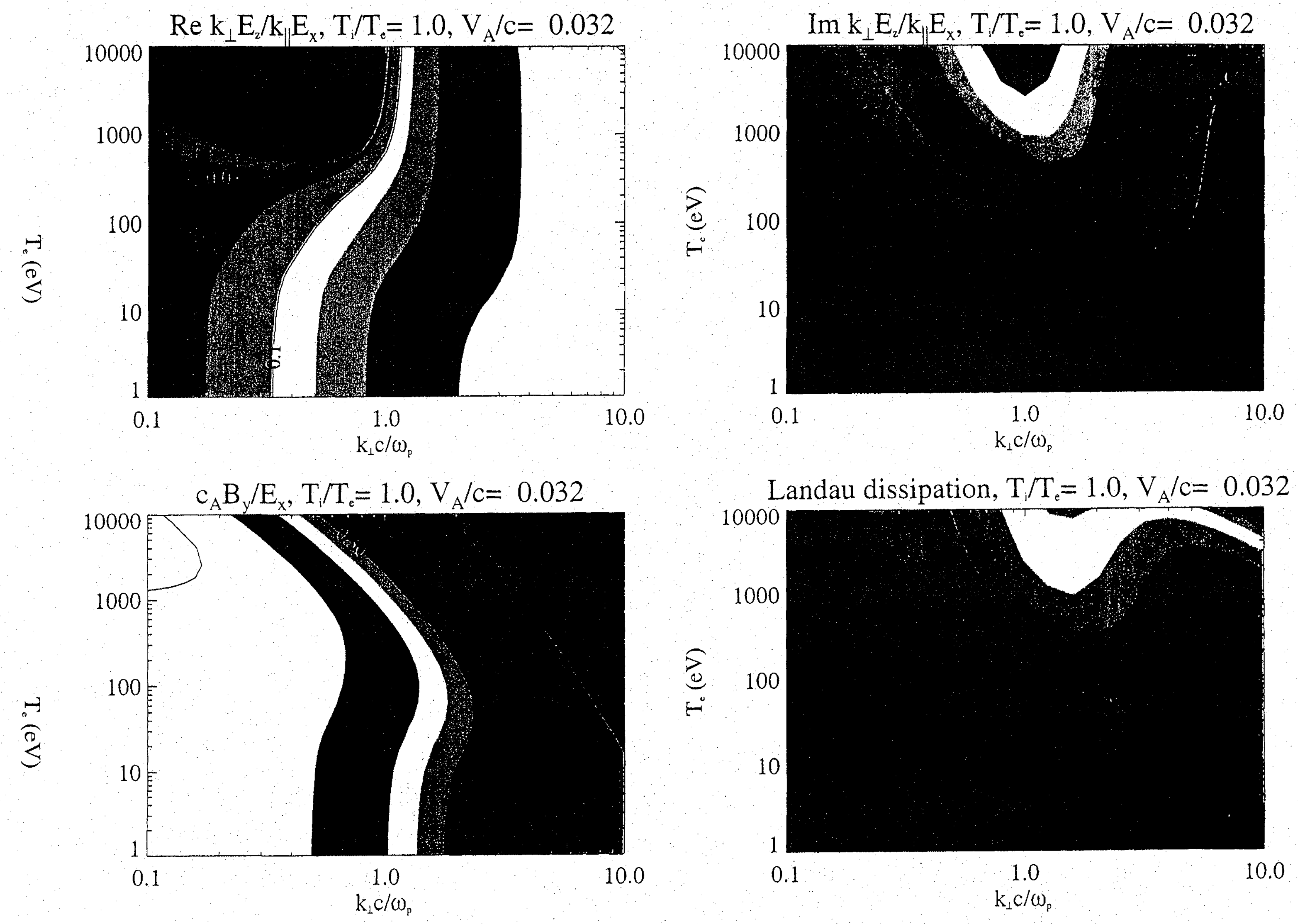

Re $k_\perp E_z/k_\parallel E_x$, T_i/T_e= 1.0, V_A/c= 0.032
10000
1000
100
10
1
T_e (eV)
0.1
1.0
10.0
$k_\perp c/\omega_p$
Im $k_\perp E_z/k_\parallel E_x$, T_i/T_e= 1.0, V_A/c= 0.032
T_e (eV)
$k_\perp c/\omega_p$
$c_A B_y/E_x$, T_i/T_e= 1.0, V_A/c= 0.032
T_e (eV)
$k_\perp c/\omega_p$
Landau dissipation, T_i/T_e= 1.0, V_A/c= 0.032
T_e (eV)
$k_\perp c/\omega_p$

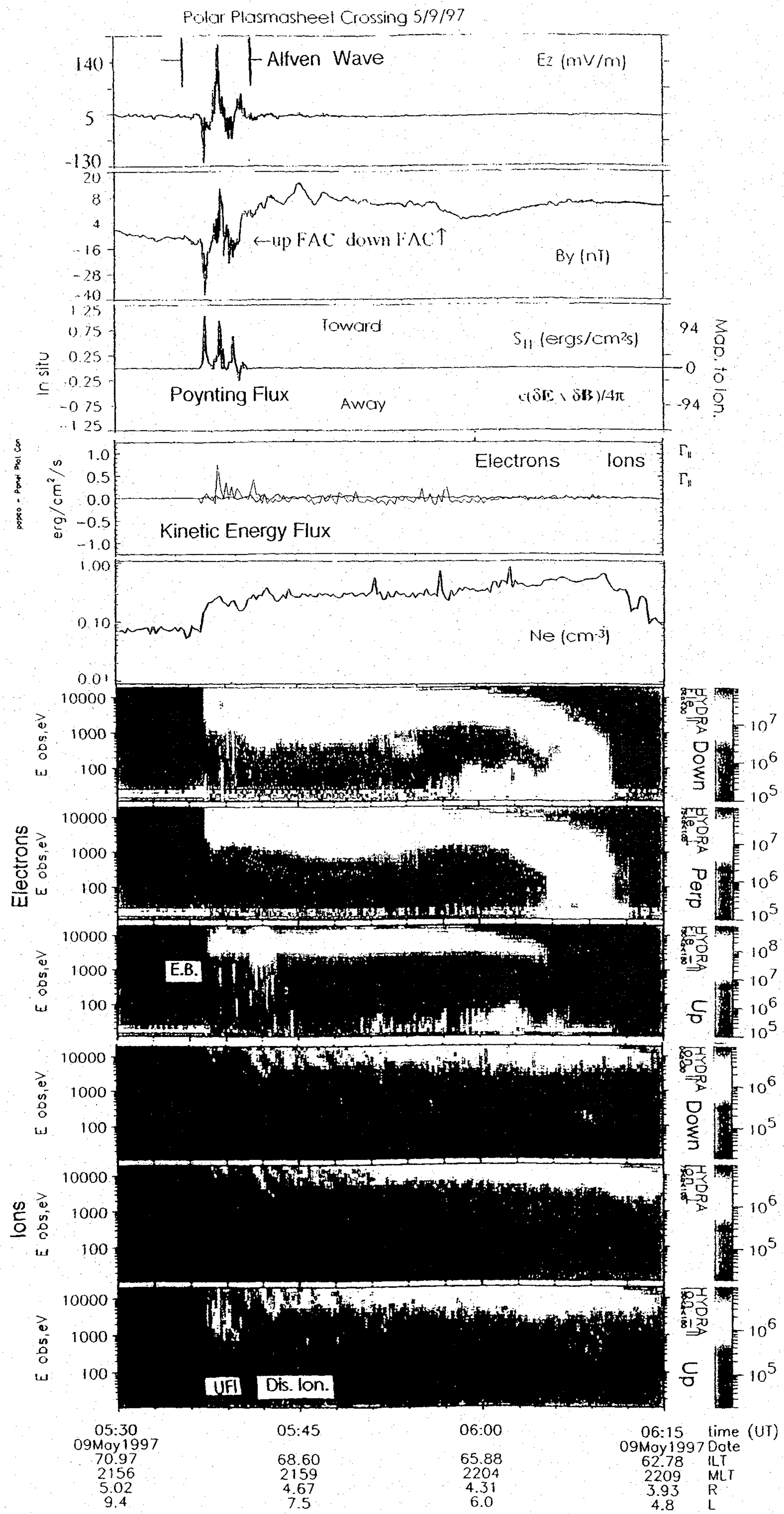

Polar Plasmasheet Crossing 5/9/97
Alfven Wave
Ez (mV/m)
←up FAC down FAC↑
By (nT)
Toward
Away
Poynting Flux
In situ
Map. to Ion.
Electrons
Ions
Kinetic Energy Flux
erg/cm²/s
Ne (cm⁻³)
E obs,eV
E.B.
HYDRA Down
HYDRA Perp
HYDRA Up
UFI
Dis. Ion.
05:30
05:45
06:00
06:15
time (UT)
09May1997
Date
ILT
MLT
R
L

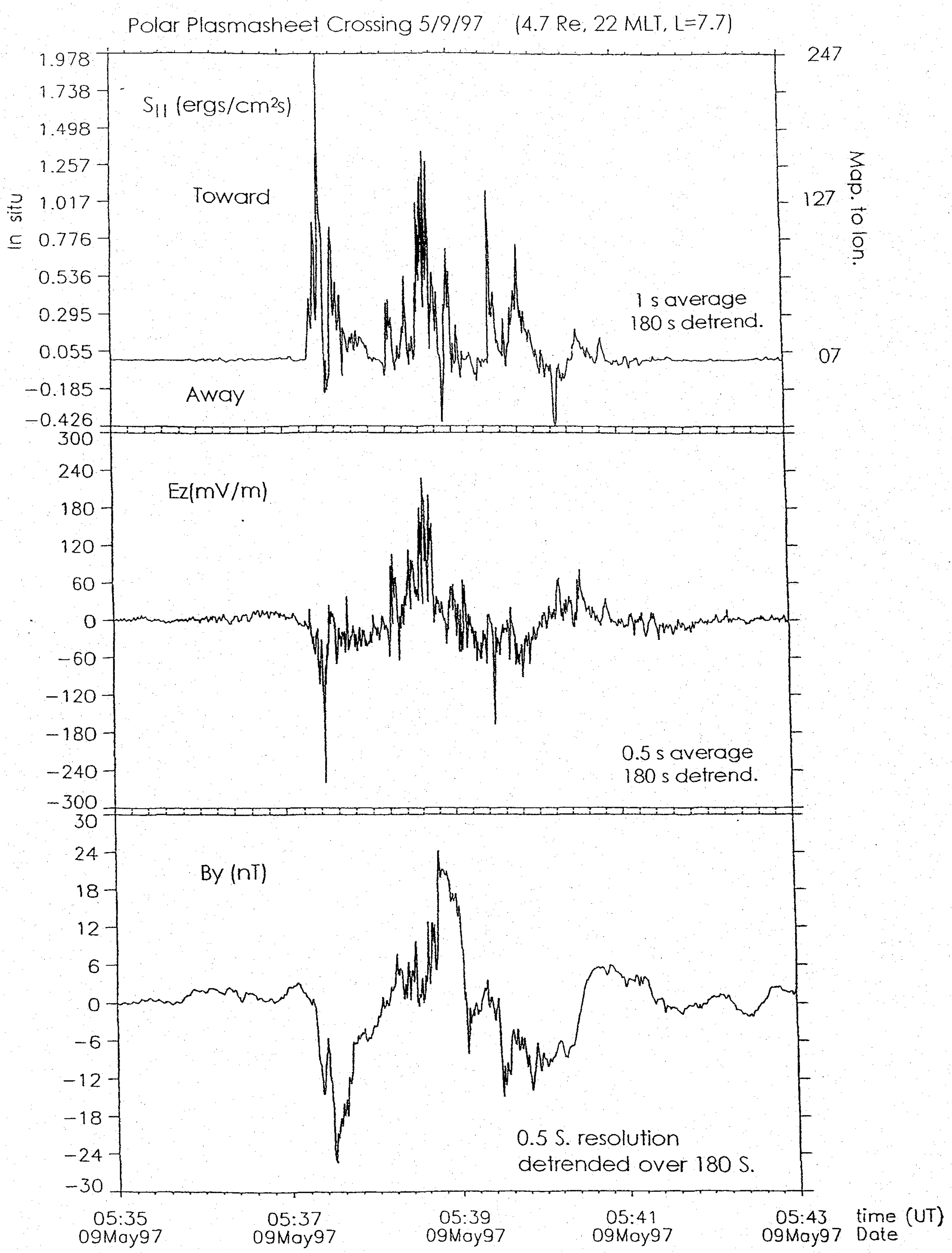

Polar Plasmasheet Crossing 5/9/97 (4.7 Re, 22 MLT, L=7.7)
1.978
1.738
1.498
1.257
1.017
0.776
0.536
0.295
0.055
−0.185
−0.426
In situ
S|| (ergs/cm²s)
Toward
Away
247
127
07
Map. to Ion.
1 s average
180 s detrend.
300
240
180
120
60
0
−60
−120
−180
−240
−300
Ez(mV/m)
0.5 s average
180 s detrend.
30
24
18
12
6
0
−6
−12
−18
−24
−30
By (nT)
0.5 S. resolution
detrended over 180 S.
05:35 09May97
05:37 09May97
05:39 09May97
05:41 09May97
05:43 09May97
time (UT)
Date

Figure 3

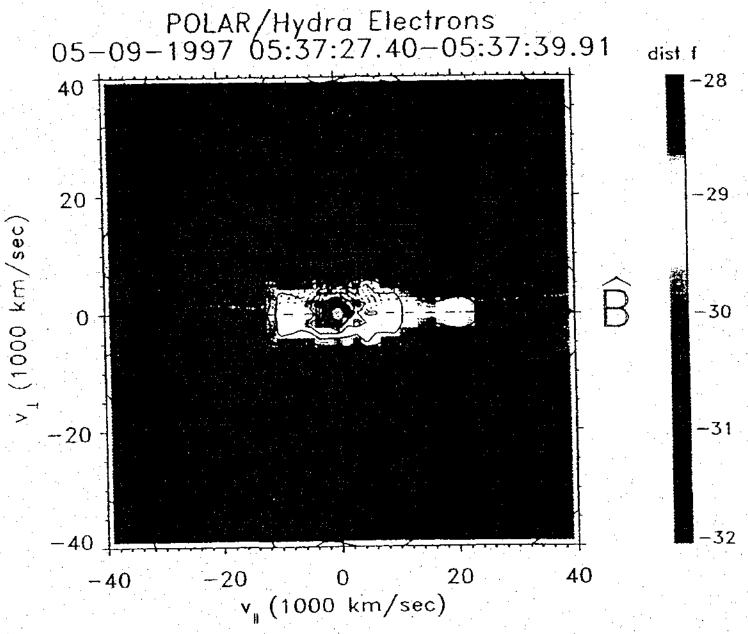
POLAR/Hydra Electrons
05-09-1997 05:37:27.40-05:37:39.91
dist f
-28
-29
-30
-31
-32
40
20
0
-20
-40
-40
-20
0
20
40
$v_\perp$ (1000 km/sec)
$v_\parallel$ (1000 km/sec)
$\hat{B}$

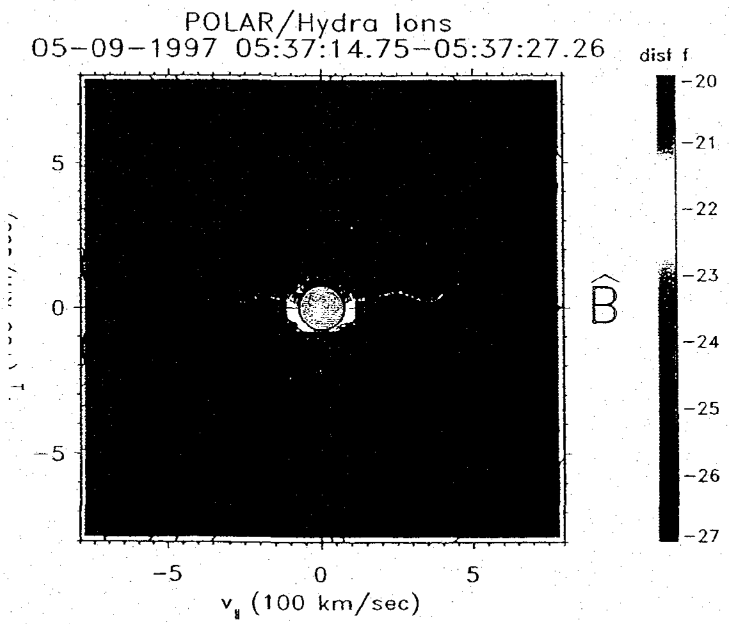
POLAR/Hydra Ions
05-09-1997 05:37:14.75-05:37:27.26
dist f
-20
-21
-22
-23
-24
-25
-26
-27
5
0
-5
-5
0
5
$v_\parallel$ (100 km/sec)
$\hat{B}$

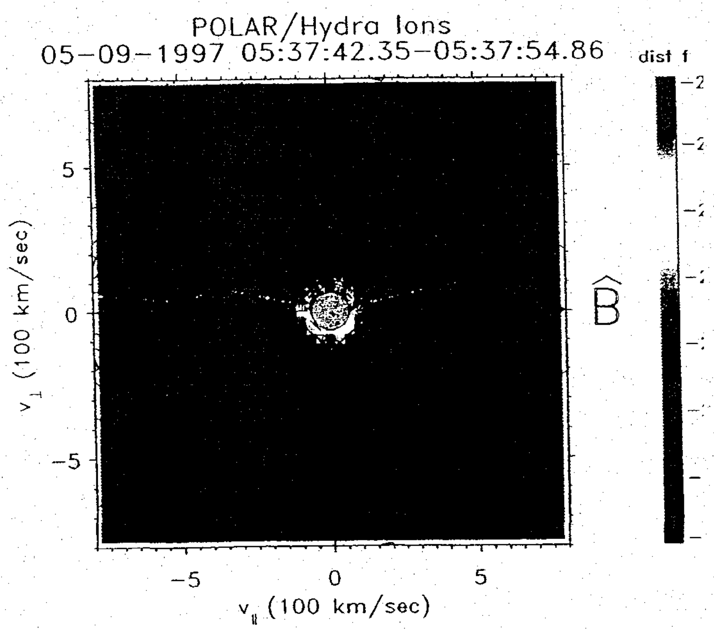
POLAR/Hydra Ions
05-09-1997 05:37:42.35-05:37:54.86
dist f
5
0
-5
-5
0
5
$v_\perp$ (100 km/sec)
$v_\parallel$ (100 km/sec)
$\hat{B}$

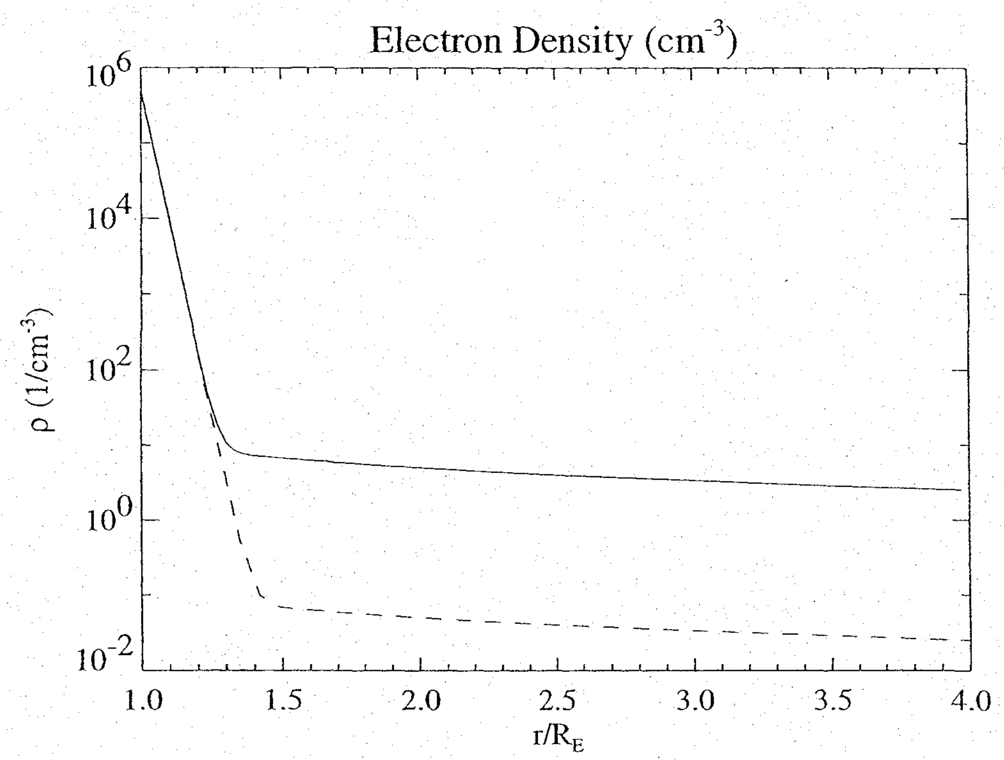
Electron Density (cm-3)
10^6
10^4
10^2
10^0
10^-2
ρ (1/cm-3)
1.0
1.5
2.0
2.5
3.0
3.5
4.0
r/R_E

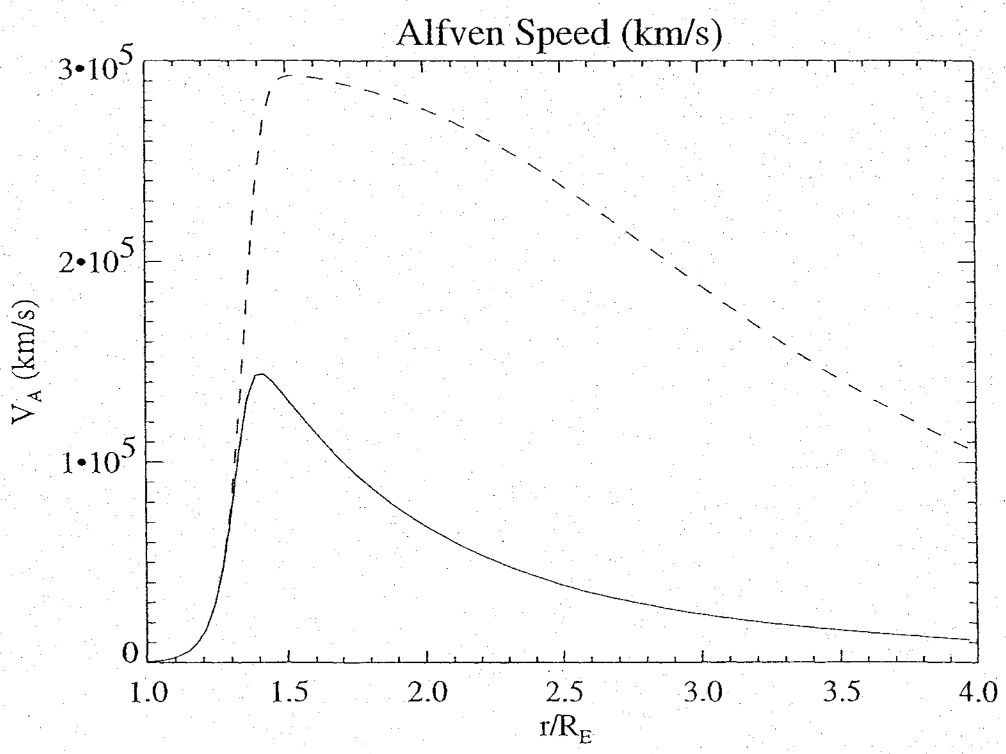
Alfven Speed (km/s)
3•10^5
2•10^5
1•10^5
0
V_A (km/s)
1.0
1.5
2.0
2.5
3.0
3.5
4.0
r/R_E

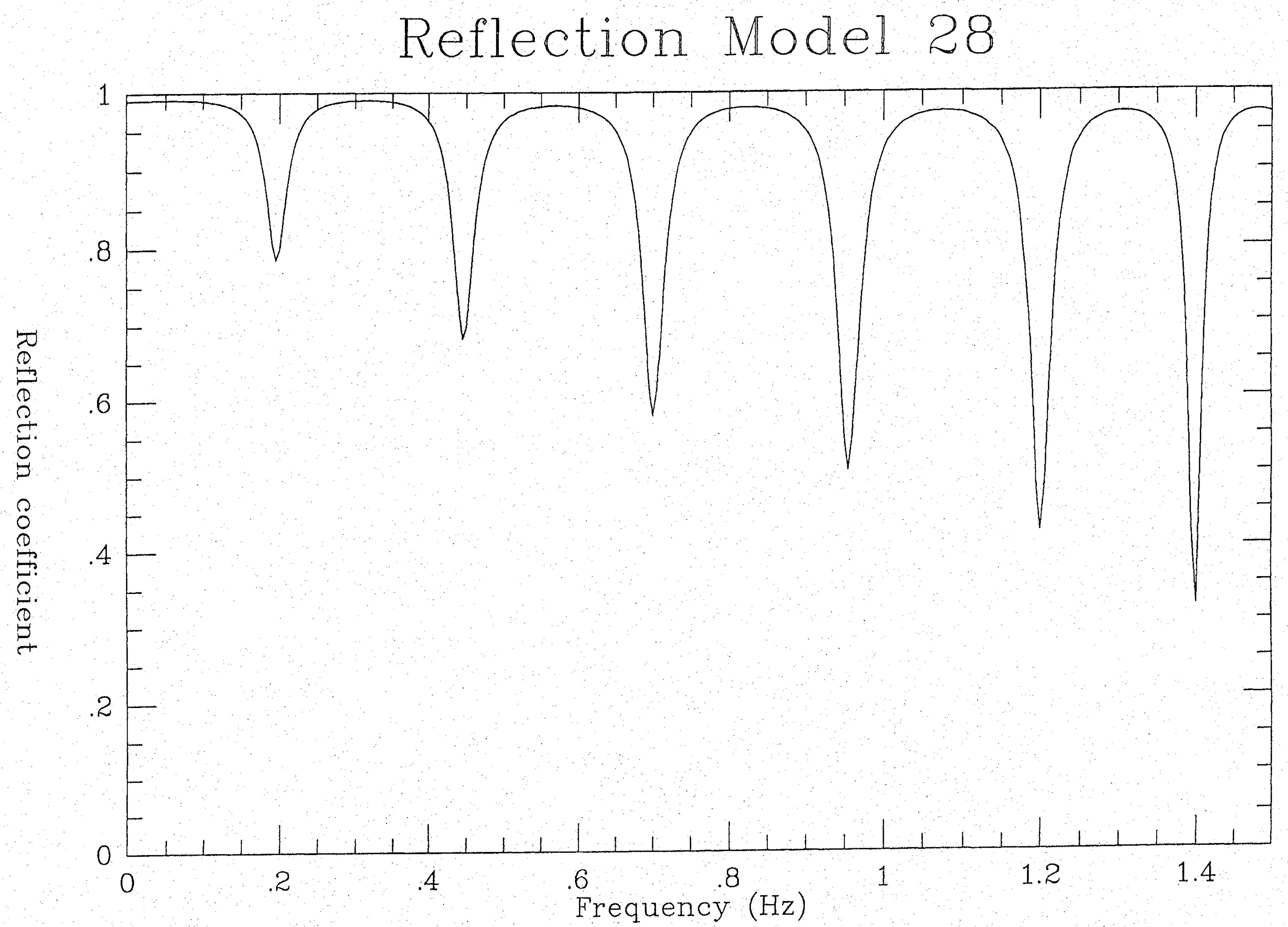
Reflection Model 28
Reflection coefficient
Frequency (Hz)
0
.2
.4
.6
.8
1
1.2
1.4

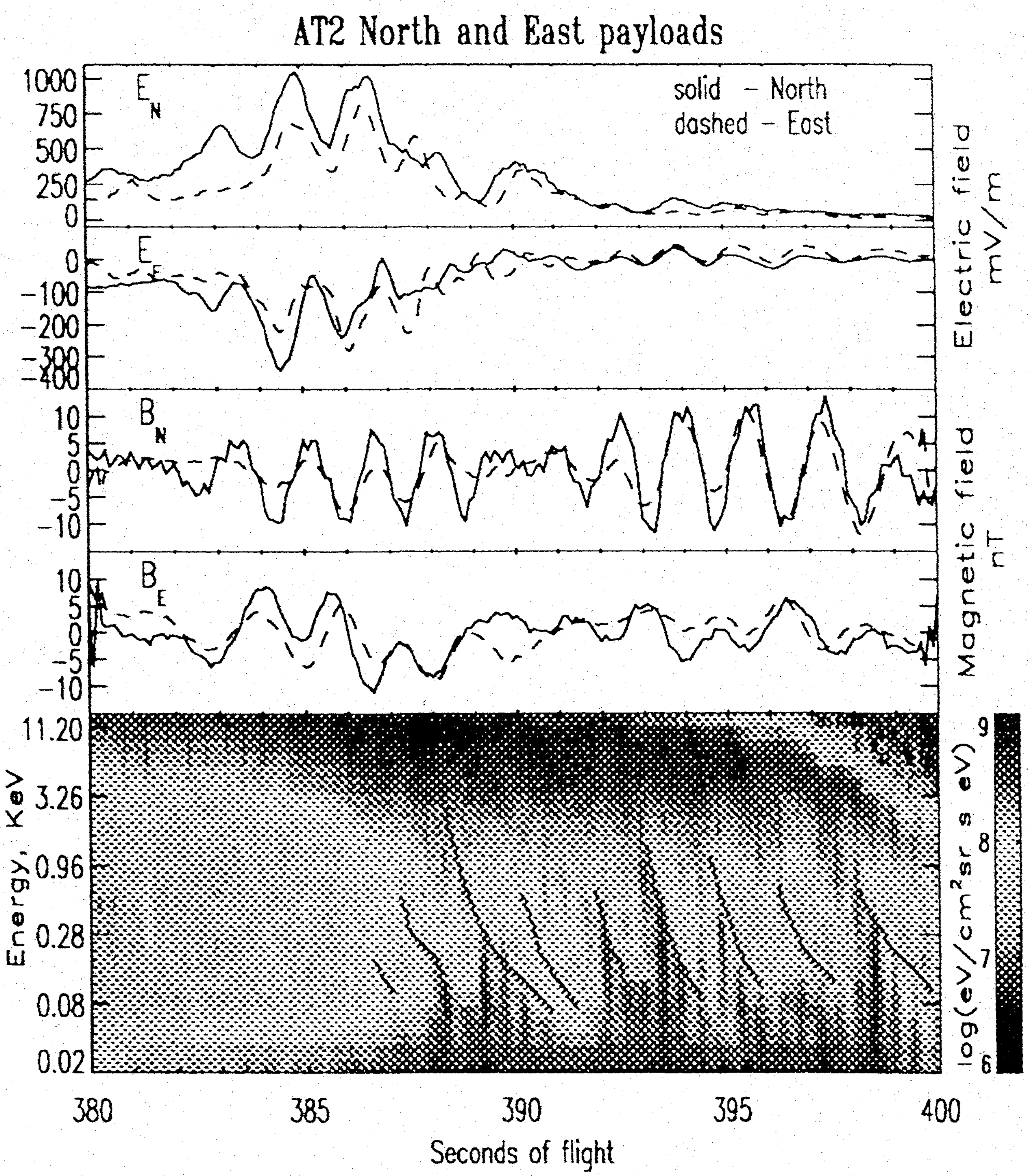

Figure 1. Electric and magnetic fields from the East and North payloads in the geographical coordinates. Lower panel - electron spectrogram with overlaid dispersion traces.

MAGNETIC PULSATION (PiB) KILPISJÄRVI

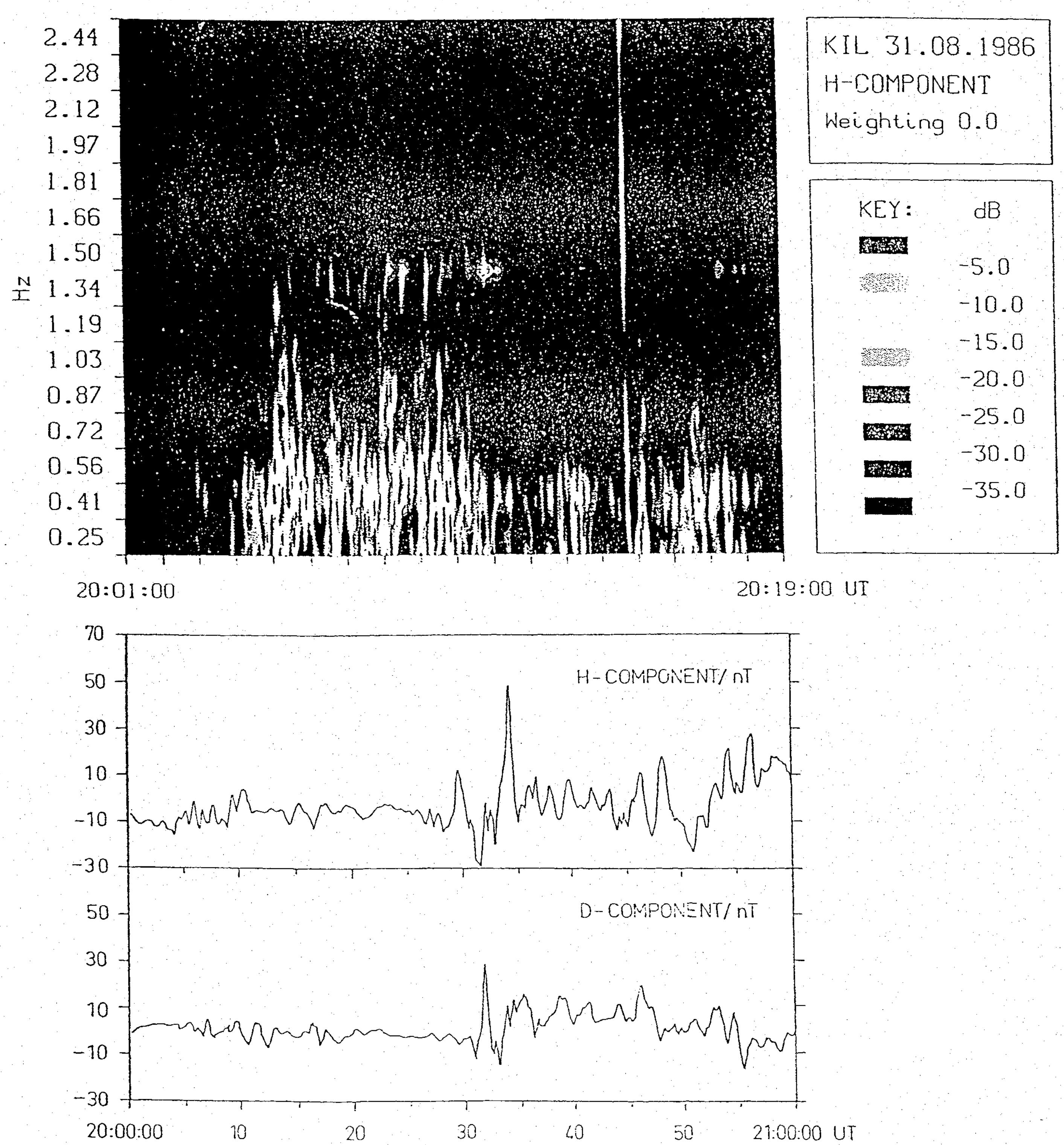

Koskinen et al, 93

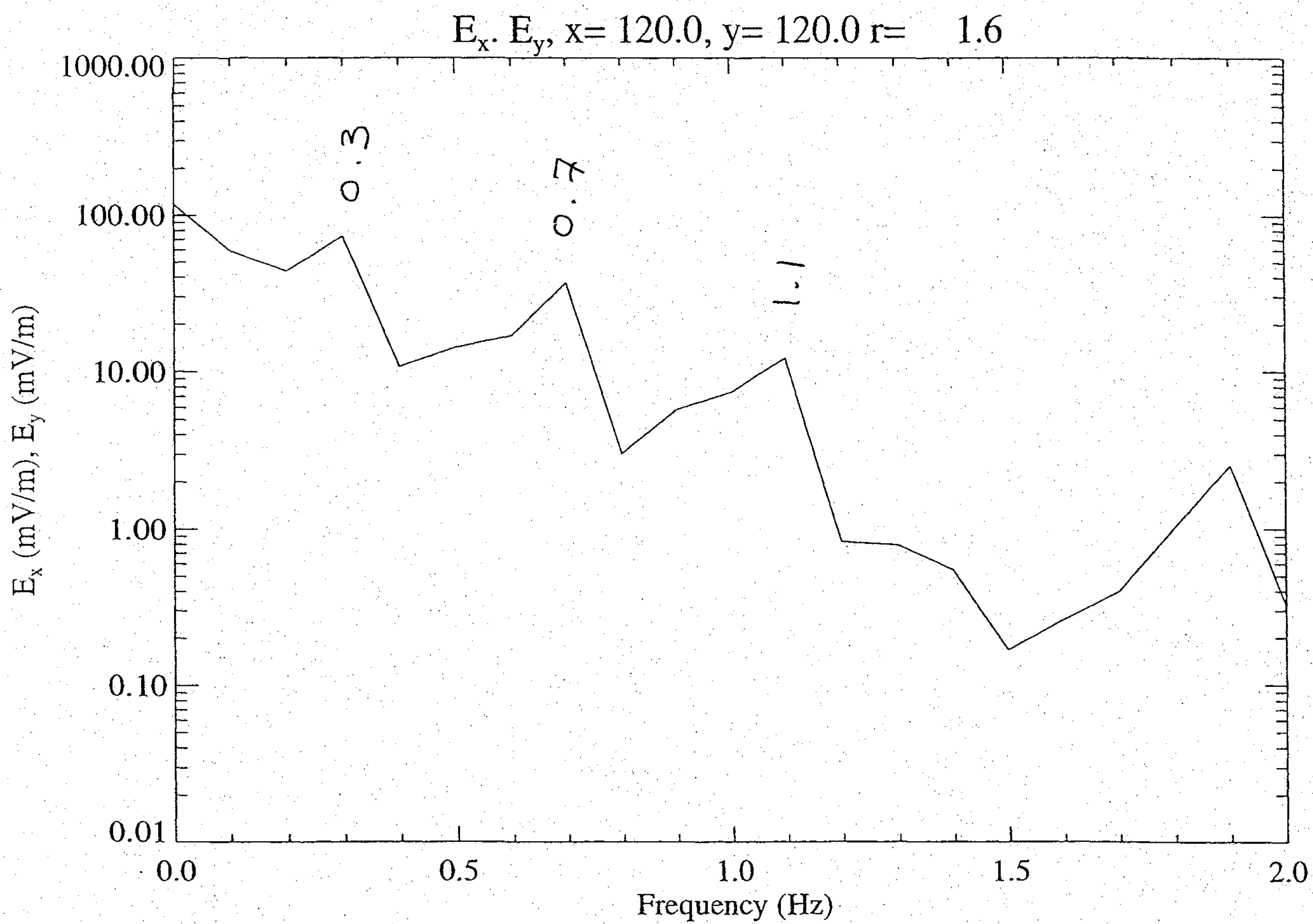

Ex. Ey, x= 120.0, y= 120.0 r= 1.6
1000.00
100.00
10.00
1.00
0.10
0.01
Ex (mV/m), Ey (mV/m)
0.0
0.5
1.0
1.5
2.0
Frequency (Hz)
0.3
0.7
1.1

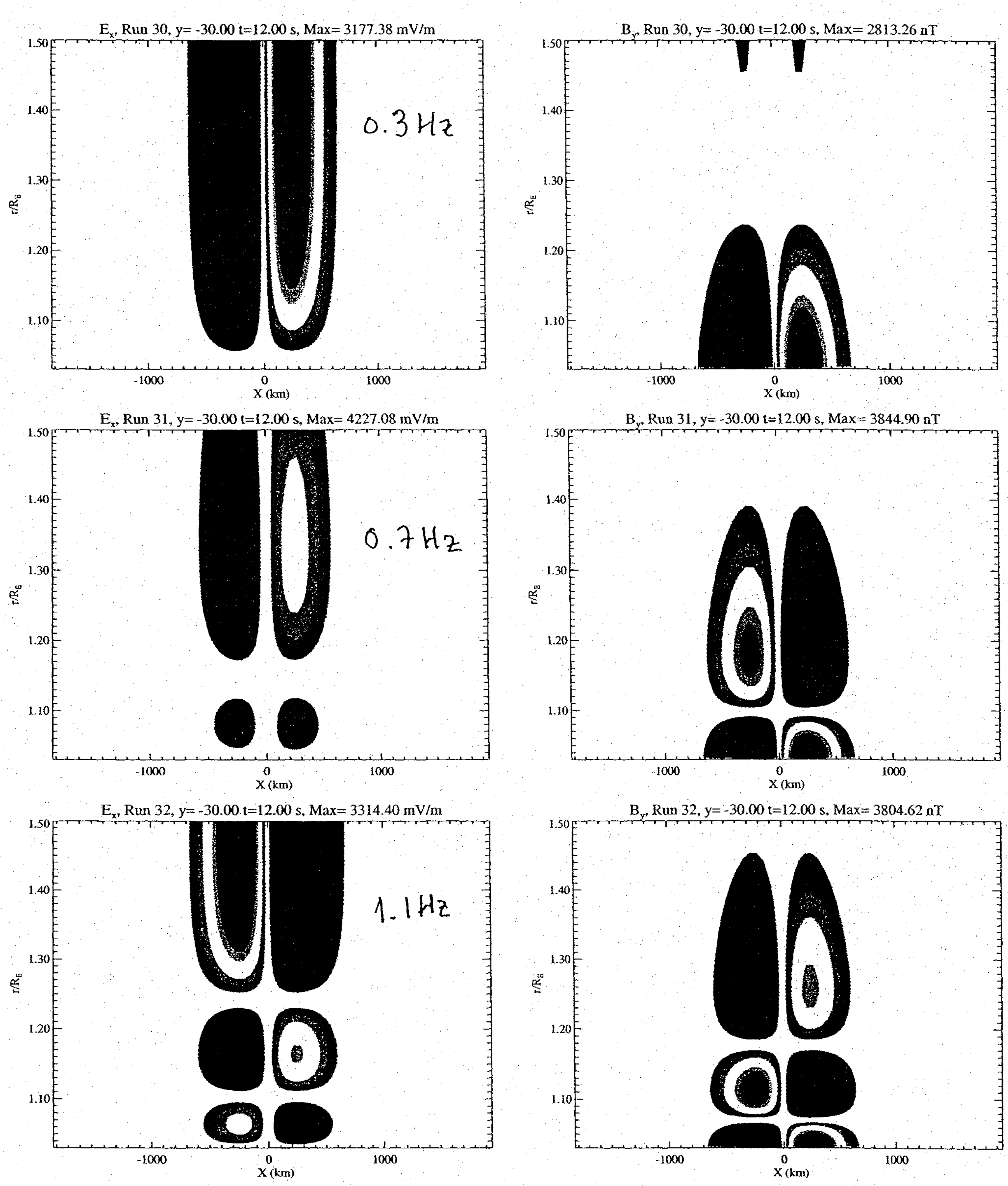
E$_x$, Run 30, y= -30.00 t=12.00 s, Max= 3177.38 mV/m
0.3 Hz
B$_y$, Run 30, y= -30.00 t=12.00 s, Max= 2813.26 nT
E$_x$, Run 31, y= -30.00 t=12.00 s, Max= 4227.08 mV/m
0.7 Hz
B$_y$, Run 31, y= -30.00 t=12.00 s, Max= 3844.90 nT
E$_x$, Run 32, y= -30.00 t=12.00 s, Max= 3314.40 mV/m
1.1 Hz
B$_y$, Run 32, y= -30.00 t=12.00 s, Max= 3804.62 nT
r/R$_E$
X (km)
1.10
1.20
1.30
1.40
1.50
-1000
0
1000